UNIVERSITY OF OKLAHOMA

GRADUATE COLLEGE

ENHANCED RADAR DETECTION BASED ON A WEATHER-AWARE CONSTANT FALSE ALARM RATE ALGORITHM

A THESIS

SUBMITTED TO THE GRADUATE FACULTY

in partial fulfillment of the requirements for the

Degree of

MASTER OF SCIENCE

By

BREANNA MAPES
Norman, Oklahoma
2025

ENHANCED RADAR DETECTION BASED ON A WEATHER-AWARE
CONSTANT FALSE ALARM RATE ALGORITHM

A THESIS APPROVED FOR THE
SCHOOL OF ELECTRICAL AND COMPUTER ENGINEERING

BY THE COMMITTEE CONSISTING OF

Dr. Robert Palmer, Chair

Dr. David Schvartzman Cohenca

Dr. Mark Yeary

Dedicated to my sister, Audrey.

Acknowledgments

I would like to begin by thanking my advisor Dr. Bob Palmer for his guidance during my time at the ARRC. I am thankful for his patience and the time and effort he dedicated to mentoring me. I would also like to thank my committee members, Dr. David Scvhartzman and Dr. Mark Yeary, who provided so much helpful feedback throughout my time here. I am incredibly grateful for their insight.

Of course, I would be remiss to exclude the people who kept life fun when I was stuck in my research. My ARRC squad, Lucía, Cody, and Sam provided much needed breaks during the work day including the lunch tradition of Guitar Hero and the crossword, as well as the occasional walk. Thank you for keeping things fun while we stressed. Noël, I am eternally thankful for weekly game nights that turned into drama watch parties and learning Thai together. To my book club friends, thank you for our weekly discussions and passionate debates.

My family and friends have my endless thanks for their support. I am thankful for all their encouragement and support as I continued my education. I would especially like to thank my sister, who was a tremendous help and source of encouragement as I wrote. Finally, I would like to thank my fiancé Adam for his unwavering support and encouragement, and who made sure I was prioritizing myself, too. I appreciate you endlessly.

Table of Contents

List of Tables

List of Figures

Abstract

The multifunction phased array radar (MPAR) program was created by organizations including the Federal Aviation Administration (FAA) and the National Oceanic and Atmospheric Administration (NOAA) in an attempt to reduce overall cost by combining the missions of multiple agencies. Required capabilities for this project include detection of both civilian point targets and weather. One benefit of a combined radar for both agencies is the potential to improve detection within a storm. In detection for a point target, the presence of weather is considered clutter. The presence of strong weather clutter limits the abilities of traditional detection algorithms to detect weaker targets, and causes an increase in false alarms. The weather-aware constant false alarm rate (Wx-CFAR) algorithm is proposed as a mitigation path for detection in weather clutter. This algorithm combines the use of traditional constant false alarm rate (CFAR) techniques with additional variables calculated from weather. It uses a decision tree in order to determine if there is clear air or weather clutter. This algorithm is aimed at improving detection within a storm, and lowering the number of false alarms due to increased clutter. The algorithm was demonstrated on single polarization data which was collected using Horus with light precipitation and multiple aircraft present throughout. The results show a decrease in false alarms while maintaining an improved number of detections. The algorithm presented limitations when a point target had a similar radial velocity to the surrounding clutter and when a point target was located along a clutter edge.

Chapter 1

Introduction

1.1 Background

The concept of radar was first demonstrated between 1885 and 1888 when Heinrich Hertz verified James Clerk Maxwell's electromagnetic field theory via a series of experiments. The first instance of radar use occurred in 1904, when Hertz created a monostatic pulse radar [1]. Although the addition of ranging did not occur until 1924, there were several uses of radar detection in years prior. In 1915, Sir Watson-Watt used radar for thunderstorm warnings, which began the use of radar for meteorological purposes. His work in the 1930s was the beginning of using radar to detect weather, as it was determined to have a vital role for aviation. World War II further advanced the usage of radar in detection and tracking of enemy aircraft in the 1930s and 1940s. In 1940, the term 'radar' was officially coined and accepted [2].

Since the initial meteorological use of radar during WWII, the capabilities of weather radar has expanded greatly. In 1944, the first radar network for weather surveillance was implemented, quickly followed by a second. It was not until after WWII that true weather radar began development, and was in use as a temporary solution until the 1960s. In the 1950s, radar use began for identifying severe storms such as tornadoes and hurricanes. In the 1980s and 1990s, the Weather Surveillance Radar-1988 Doppler (WSR-88D) was developed to include Doppler capabilities for weather radar [3]. This introduction helped severe weather be predicted more accurately, and is crucial to weather radar today. By 2013, the WSR-88D was upgraded to include dual polarization capabilities, which provided great improvements to the classification of scatterers. [4].

The development of tracking radar also truly began during WWII, as the necessity to detect enemy aircraft arose. After the war, commercial use of aircraft was desired, requiring better regulations and safety standards. By 1950, the Airport Surveillance Radar-1 (ASR-1) was in place [5]. After the birth of the Federal Aviation Administration (FAA) in 1958, the United States began regulating its airspace on a federal level. The need for air traffic control (ATC) was expanding to create a more safe and efficient method of travel, and the automated radar traffic control system (ARTS) was developed in the 1960s [6]. At present, the Airport Surveillance Radar-11 (ASR-11) is used for ATC and the monitoring of weather conditions [7].

The primary goals of weather radar are to detect and track meteorological artifacts, and see conditions in advance for potential severe weather. Monitoring the environmental conditions, providing reliable predictions, and updates on the current weather conditions are crucial for meteorological radar. For the aviation industry, radar is used to ensure that the location of aircraft is managed and accidents are prevented. It is also used for detection of non-cooperative aircraft, and meteorological purposes.

1.1.1 Multifunction Phased Array Radar Project

The multifunction phased array radar (MPAR) project started in the early 2000s to create one radar with the functionality to handle the needs of various agencies such as the FAA and the National Oceanic and Atmospheric Administration (NOAA), including ATC, weather surveillance, and non-cooperative air surveillance [8]. [8] proposes several potential uses for an MPAR network outside of these three key functionalities, including observing aviation hazards like birds, airborne toxic materials, smoke from wildfires, and more. Although a multifunctional radar is possible, there are challenges that come with combining the missions of these agencies. Weather radar requires dual polarization to gain important information such as hydrometeor classification, and although this is not technically required for aircraft focused radar, it could still be beneficial [9]. Furthermore, NOAA needs to replace the WSR-88D, which were developed in 1988 and will be reaching end of life soon; new radar must replace them by 2040 [10]. If this project successfully determines a suitable replacement, then the MPAR network would replace the WSR-88D network, the FAA Terminal area radar, and the United States Air Force (USAF)/FAA long range radar [11].

The initial architecture proposed for the MPAR project was four fixed planar faces which covered 90 degrees in azimuth for each face. Although this design would be beneficial for all requirements of the program, it is not the most feasible in terms of affordability. Alternative architectures include the Cylindrical Polarimetric Phased Array Radar (CPPAR) project developed by the Advanced Radar Research Center (ARRC) at the University of Oklahoma, and the Advanced Technology Demonstrator (ATD) developed by MIT Lincoln Labs [9]. The CPPAR poses unique challenges due to its architecture, and nearly achieves the performance targets of this project [12]. The ATD was installed in 2019 and met the expectations needed for the MPAR project for each performance target tested [13]. Another alternative solution for this project is Horus, a fully digital polarimetric phased array radar developed by the ARRC at the University of Oklahoma.

The Horus radar has the capabilities of performing multiple missions as set out by the MPAR project [14]. Horus is a planar, phased array, "software defined radar," which means that it is future proof [10]. Since weather radar is a rapidly evolving field and new technology is becoming increasingly important in the field for observing the development of quickly evolving storms, Horus being digital and heavily software based allows for cost savings when future upgrades may arise. The MPAR project could also benefit from using Horus because of the accuracy this radar provides. Additionally, Horus is a dual polarimetric radar, meaning that it can scan in both horizontal (H) and vertical (V) polarization.

1.2 Motivation

One of the primary functions of radar in regards to aircraft is detection. Two of the three required functionality for the MPAR project mentioned in Section 1.1.1 focus on detection of point targets, primarily for the aviation industry with a goal to improve aviation safety. The Horus radar is primarily used for weather detection, which covers the third required functionality. To prove the utility in using Horus for all operations, detecting aircraft and other non-meteorological targets both inside and outside of a storm would show simultaneous capabilities of all major functionality.

Detection algorithms typically only use returned power to detect spikes in the data for identifying potential targets. This becomes tricky if there is weather present along with the target, as the power will also increase where more hydrometeors are located. The target may still be located, but the meteorological echoes may cause false alarms and make it harder to locate. With the use of a weather radar, the ability to include additional parameters that would already be computed opens up the potential for enhanced detection. It is possible to combine multiple variables to improve upon a detection algorithm and negate additional false alarms which arise from the added weather. The idea behind using additional weather radar variables in detection is to improve the confidence of the detection and thus decrease false alarm rate.

1.3 Contributions and Outline

This thesis aims to prove the utility in using weather variables to detect non-meteorological targets through the use of real data including both real and simulated targets in both weather and clear air. Furthermore, it aims to improve traditional detection algorithms by augmenting those algorithms with weather data.

The rest of this thesis is organized as follows: in Chapter 2, a brief review of the signal flow in a weather radar is given, along with an overview of the various radar variables used. In Chapter 3, there is a review of detection and various techniques utilized in this thesis. Chapter 4 goes through the process behind the detection techniques presented. This will include a description of the data used, techniques employed prior to running a detection algorithm, and the results of using various weather variables separately and combined for a detection algorithm. Finally, the weather-aware constant false alarm rate (Wx-CFAR) algorithm is defined. Chapter 5 compares the separate and combined detection algorithm results and provides an analysis of the Wx-CFAR algorithm. Benefits and limitations of the algorithm will be discussed. Finally, Chapter 6 concludes this paper and future work is outlined.

Chapter 2

Review of Weather Radar

Weather radar has been in use since the 1940s when it was developed during WWII. Since then, it has expanded to be used for many purposes, including monitoring severe weather conditions in real time. It is also beneficial for the research of why storms form, so that watches can be issued in advance when the conditions are present. There are many different frequency bands where weather radar may operate, including S-band (2-4 GHz), C-band (4-8 GHz), and X-band (8-12.5 GHz). S-band is commonly used for weather as it can detect far ranges with higher unambiguous velocities. Its scatter is also Rayleigh, which enhances interpretation of the returned echoes. X-band is useful for shorter-range radar but is plagued by poor Doppler ambiguity performance. The network of weather radars in the United States is comprised of the WSR-88D, a Doppler radar which operates at S-band [15].

2.1 Signal Flow

In a typical weather radar, key components include the waveform generator, transmitter, antenna, and receiver [2]. The signal is first generated from the Stable Local Oscillator (STALO) at the desired frequency. In a pulsed radar such as Horus or the WSR-88Ds, this is then modulated to produce a pulsed waveform. The STALO outputs at an extremely low power, so the pulsed waveform is next sent to an amplifier to increase the output to a desired power. It is then sent through a transmit switch to the antenna. What the antenna receives back is sent through the receive switch and mixed with the original signal from the STALO. It is demodulated by mixing at $0°$ and $90°$ to produce in-phase and quadrature (IQ) signals and filtering to remove the carrier frequency. The I and Q signals take the following form [2]:

$$I(t) = \left(\frac{|A|}{\sqrt{2}}\right) U(t - 2r/c) cos(4\pi r/\lambda - \psi_t - \psi_s) \tag{2.1a}$$

$$Q(t) = \left(\frac{-|A|}{\sqrt{2}}\right) U(t - 2r/c) sin(4\pi r/\lambda - \psi_t - \psi_s) \tag{2.1b}$$

where A is the complex amplitude, $2r/c$ is the range time, ψ_t is the transmitter phase, and ψ_s is the phase shift from scattering. These signals can be expressed as the echo signal using a complex sum [2]:

$$V(t, r) = Ae^{j2\pi f(t-2r/c)+j\psi} U(t - 2r/c) = I + jQ \tag{2.2}$$

A basic diagram of this flow can be seen in Figure 2.1. To utilize the IQ signals, the derivation of the weather radar equation and other useful equations is provided. Start with incident power on the target [2]:

$$S_i = \frac{P_t g_t f^2(\theta, \phi)}{4\pi r^2} \tag{2.3}$$

where P_t is the peak power transmitted, g_t is the transmitter gain, and $f^2(\theta, \phi)$ is the normalized one way power density pattern for the antenna, which can be expressed as [2]

$$f^2(\theta, \phi) = \frac{S(\theta)}{S(0)} = \left\{ \frac{8J_2[(\pi D_a sin\theta)/\lambda]}{[(\pi D_a sin\theta)/\lambda]^2} \right\}^2 \tag{2.4}$$

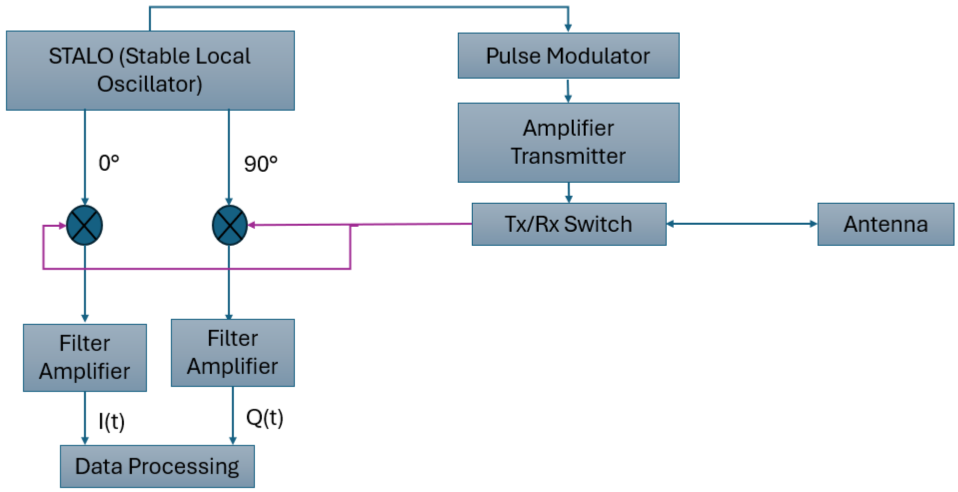

Figure 2.1: Basic block diagram of a signal flow in a radar system. The signal begins at the STALO, goes through the pulse modulator into the amplifier transmitter, then into the transmit and receive switch out to the antenna, back to the transmit and receive switch. It then goes through a mixer to demodulate the signal. The demodulated signal is sent through a filter amplifier to produce IQ signals, which are then ready for data processing.

In this equation, θ is the angular distance from the beam axis, J_2 is the second order Bessel function, and D_a is the diameter of the antenna. The returned echo power density S_r is found to be [2]

$$S_r(\theta, \phi) = \frac{P_t g_t f^2(\theta, \phi)\sigma_b}{(4\pi r^2)^2 l^2} \tag{2.5}$$

where σ_b is the backscatter cross section of a point scatterer and l is the loss. The effective collection area is written as [2]

$$A_e(\theta, \phi) = (g_r \lambda^2 / 4\pi) f^2(\theta, \phi) \tag{2.6}$$

where $g_r = g_t = g$ if the same antenna is used for transmission and reception, and P_t and P_r are measured at the same place in the antenna. Using the effective collection area and the echo power density, the received echo power is computed [2]:

$$P_r = S_r(\theta,\phi)A_e(\theta,\phi) = \frac{P_t g^2 \lambda^2 \sigma_b f^4(\theta,\phi)}{(4\pi)^3 r^4 l^2} \tag{2.7}$$

This is known as the radar equation for a point target. Another form of this equation is expressed as [1]

$$r_{max} = \left[\frac{P_t g A_e \sigma}{(4\pi)^2 S_{min}}\right]^{1/4} \tag{2.8}$$

where the maximum radar range is given as r_{max} and the minimum detectable signal is S_{min}. Additionally, the radar cross section (RCS) σ is considered here for the point target. It is useful to know these parameters for detection of a point target. There are additional forms of the point target radar equation, the first of which accounts for the noise in the received signal. To compute this, the noise figure must first be defined as [1]

$$F_n = \frac{N_{out}}{kT_0\beta g_a} = \frac{S_{in}/N_{in}}{S_{out}/N_{out}} \tag{2.9}$$

where k is Boltzmann's constant $1.38\times10^{-23}\ J/deg$, T_0 is the standard temperature $290\ K$, β is the half-power bandwidth, g_a is the available gain, S_{in} is the input signal, N_{in} is the input noise in an ideal receiver, S_{out} is the output signal of the receiver, and N_{out} is the output noise of the receiver. Understanding that S_{in} may be replaced with S_{min} if the output signal and noise powers are also set to the minimum detectable signal-to-noise ratio (SNR), then by substituting Equation (2.9) into Equation (2.8), the radar equation for a point target becomes

$$r_{max} = \left[\frac{P_t g A_e \sigma}{(4\pi)^2 kT_0\beta F_n (S/N)_{min}}\right]^{1/4} \tag{2.10}$$

When integrating over multiple pulses, the integration efficiency must also be considered. This can be defined as [1]

$$E_i(n) = \frac{(S/N)_1}{n(S/N)_n} \tag{2.11}$$

Table 2.1: Differentiation of the Swerling Targets

Case	Correlation	n_e	Fluctuation	PDF
I	completely correlated	$n_e = 1$	scan-to-scan	$\chi^2(2)$
II	completely uncorrelated	$n_e = n$	pulse-to-pulse	$\chi^2(2)$
III	completely correlated	$n_e = 1$	scan-to-scan	$\chi^2(4)$
IV	completely uncorrelated	$n_e = n$	pulse-to-pulse	$\chi^2(4)$
V/0	-	$L_f = 1$	nonfluctuating	-

where n pulses are integrated. Using Equation (2.11), the radar equation for a point target then becomes

$$r_{max} = \left[\frac{P_t g A_e \sigma n E_i(n)}{(4\pi)^2 k T_0 \beta F_n (S/N)_1} \right]^{1/4} \tag{2.12}$$

Additionally, the target may be fluctuating, which introduces a loss factor. Representative models often used for fluctuating targets are the Swerling target models, outlined in Table 2.1. The introduced loss factor is called fluctuation loss, defined as [1]

$$L_f(n_e) = (L_f)^{1/n_e} \tag{2.13}$$

where n_e independent samples are integrated. The value for L_f comes from Figure 2.2 [1]. This leads to the final radar equation for a point target to be discussed in this thesis, taking the form

$$r_{max} = \left[\frac{P_t g A_e \sigma n E_i(n)}{(4\pi)^2 k T_0 \beta F_n (S/N)_1 (L_f)^{1/n_e}} \right]^{1/4} \tag{2.14}$$

The value for n_e to be used depends on whether the Swerling model is correlated or not. The values to be used can be found in Table 2.1. Note that for the nonfluctuating case of Swerling Case V, there is no fluctuation loss so L_f is set to 1.

Now that the point target radar equations are defined, the derivation of the weather radar

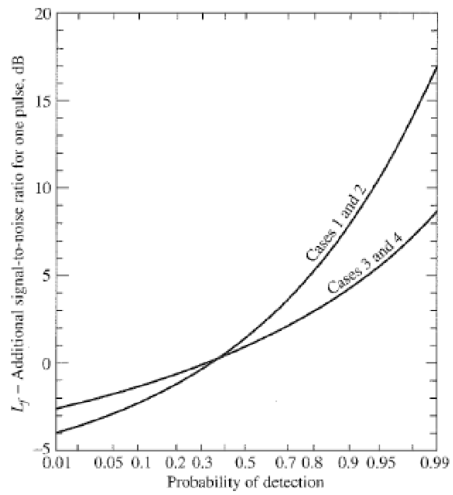

Figure 2.2: The fluctuation loss L_f for the various Swerling target models, from [1]. The X-axis represents the probability of detection (P_D) and the Y-axis represents the additional SNR (dB) required for a single pulse. This additional SNR is required for a set P_D when the target fluctuates, causing fluctuation loss.

equation may be resumed. The complex weather signal can be written as

$$V(\tau_s) = \frac{1}{\sqrt{2}} \sum_i A_i w_i e^{-j\frac{4\pi r_i}{\lambda}} \tag{2.15}$$

where w_i is the complex weighting function dependent on range, with a maximum at $r = c\tau_s/2$ and where τ_s is the pulse width. This summation is for the i^{th} scatterer. From this, the average power for a single pulse becomes

$$P(\tau_s) = V \cdot V^* = \frac{1}{2} \sum_{i,k}^{N_s} A_i A_k^* w_i w_k^* e^{j4\pi(r_k - r_i)/\lambda} \tag{2.16}$$

When looking at a resolution volume, the expected power is determined to be [2]

$$E[dP] = \frac{P_t g^2 \lambda^2 f^4(\theta - \theta_0, \phi - \phi_0)|W_s|^2 dV}{(4\pi)^3 r^4 l^2(\overrightarrow{r_0})} \frac{E[\sigma_b]}{dV} \tag{2.17}$$

where W_s is a range dependent complex weight. The reflectivity $\eta(\overrightarrow{r_0})$ is the expected backscatter per unit volume, [2]

$$\eta(\overrightarrow{r_0}) = \frac{E[\sigma_b]}{dV} = \int_0^{\infty} \sigma_b(D)N(D,\overrightarrow{r})dD \tag{2.18}$$

in which D is the diameters of the raindrops in the resolution volume. The illumination function is defined as [2]

$$I(r_0, r) = \frac{Cf^4(\theta-\theta_0, \phi-\phi_0)|W_s(r_0, r)|^2}{l^2(r)r^4} \tag{2.19a}$$

$$C = \frac{P_t g^2 \lambda^2}{(4\pi)^3} \tag{2.19b}$$

Integrating the illumination function over space gives [2]

$$P(r_0) = \int_0^{r_2}\int_0^{\pi}\int_0^{2\pi} \eta(\overrightarrow{r_0})I(r_0, r)dV \tag{2.20a}$$

$$dV = r^2\, dr\, sin\theta\, d\theta\, d\phi \tag{2.20b}$$

Under the assumption that $\eta(\overrightarrow{r_0})$ and $l(r)$ do not change much within the resolution volume, for the antenna pattern with a circularly symmetric and approximately Gaussian shape the expected value of the weather power is then [2]

$$E[P(\overrightarrow{r_0})] = \frac{P_t g^2 \eta c\tau\theta_1^2\lambda^2}{(4\pi)^3 r_0^2 l^2 16 ln(2)} \tag{2.21}$$

which is known as the weather radar equation. The half power, or -3 dB, beamwidth θ_1 is as follows [2]

$$\theta_1 = \frac{1.27\lambda}{D_a} \tag{2.22}$$

expressed in radians. The power can be used to calculate the SNR as

$$SNR = \frac{P_r}{P_n} \tag{2.23}$$

where P_r is the received power and P_n is the noise power. This concept is used to determine the quality of the data and is extremely important for detection.

The key difference between the radar equations for a point target and the weather radar equation is that the point target equations assume a singular point target in the resolution volume being examined, while the weather radar equation assumes a distributed target such as rain. This difference determines how the target is analyzed and what is important to analyze for the target. For point targets, the RCS σ is defined for one target, while the reflectivity $\eta(\overrightarrow{r_0})$ is defined for the unit volume potentially containing numerous scatterers.

2.2 Polarimetric Variables

When examining weather, there are multiple variables that are used to determine things such as the severity of the storm, if it will evolve into severe weather like tornadoes, and to classify the type of hydrometeors such as rain, hail, or graupel. Three main variables can be measured using a single polarimetric radar, including reflectivity factor (Z_{v}), radial velocity (v_{r}), and spectrum width (σ_{v}). Additional variables can be determined with a dual polarimetric radar, including differential reflectivity (Z_{DR}), correlation coefficient (ρ_{hv}), and differential phase (Φ_{DP}). Although the information provided by single polarimetric variables is extremely important, the addition of dual polarimetric variables allowed for improvements to classification of scatterers and increasing capability in severe weather warnings [4]. Because of this, most weather radar today will be dual polarimetric in nature.

The signal power in each polarization can be expressed as

$$\hat{S}_h = \frac{1}{M}\sum_{m=0}^{M-1}[V_h(m)\cdot V_h^*(m)] - P_n \tag{2.24a}$$

$$\hat{S}_v = \frac{1}{M}\sum_{m=0}^{M-1}[V_v(m)\cdot V_v^*(m)] - P_n \tag{2.24b}$$

where M is the number of samples used. The power can be found using the 0^{th} lag of the autocorrelation function (ACF), which can be found for either polarization with

$$\hat{R}(T_s) = \frac{1}{M}\sum_{m=0}^{M-1} V^*(m)V(m+1) \tag{2.25}$$

In this case, T_s is the pulse repetition time (PRT).

2.2.1 Single Polarimetric Variables

The reflectivity factor, commonly referred to as reflectivity (Z_{v}), is the relation of the drop size diameter to reflectivity $\eta(\overrightarrow{r_0})$ and is used to determine intensity and location of a storm. If Rayleigh scattering does not apply, this relationship is expressed as [2]

$$\eta(\overrightarrow{r_0}) = \frac{\pi^5}{\lambda^4}|K_w|^2 Z_e \tag{2.26}$$

where K_w is the specific attenuation for the hydrometeor type and a known constant, and Z_e is the equivalent reflectivity factor. This can be related to the power by substituting Equation (2.26) into Equation (2.21), getting

$$Z_e = \frac{l^2 r_0^2 P(\overrightarrow{r_0})}{C} \tag{2.27a}$$

$$C = \frac{P_t g^2 c\tau\pi^6\theta_1^2}{(4\pi)^3\lambda^2 16 ln2}|K_w|^2 \tag{2.27b}$$

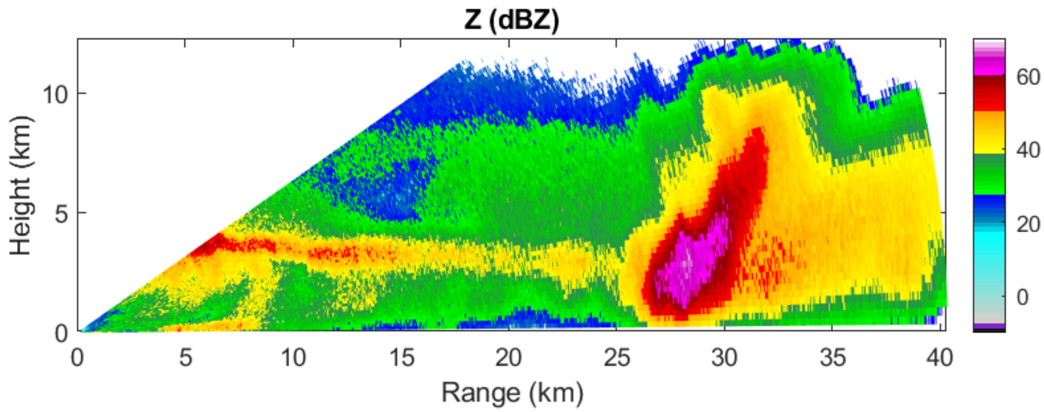

Figure 2.3: A Range Height Indicator (RHI) scan of Z_{v} (dBZ). The data was collected in Norman, OK, on 4 October 2023 at 22:19:08 UTC using Horus.

where r_0 is the range correction and C is a system calibration constant. This is expressed in logarithmic units (dBZ) in practice, which can be calculated with

$$10log_{10}(Z_e) = 10log_{10}(P(\overrightarrow{r_0})) + 20log_{10}(l) + 20log_{10}(r_0) - 10log_{10}(C) \tag{2.28}$$

A higher value of reflectivity will typically indicate that there is heavier precipitation in that area [16]. In other cases, this may be a non-meteorological target such as aircraft or buildings. A plot of Z_{v} can be found in Figure 2.3.

Radial velocity (v_{r}), or Doppler velocity, is the velocity of the storm relative to the radar, and is the first moment of the power normalized spectra, which can be found using the phase change between pulses as follows

$$v_r = \frac{-\lambda}{4\pi T_s} \angle \left(\hat{R}(T_s) \right) \tag{2.29}$$

where $\angle(\hat{R}(T_s))$ is the angle of the ACF at the first lag. Some aliasing can be seen in the velocity plot found in Figure 2.4 above 5 km in height. This is due to the maximum

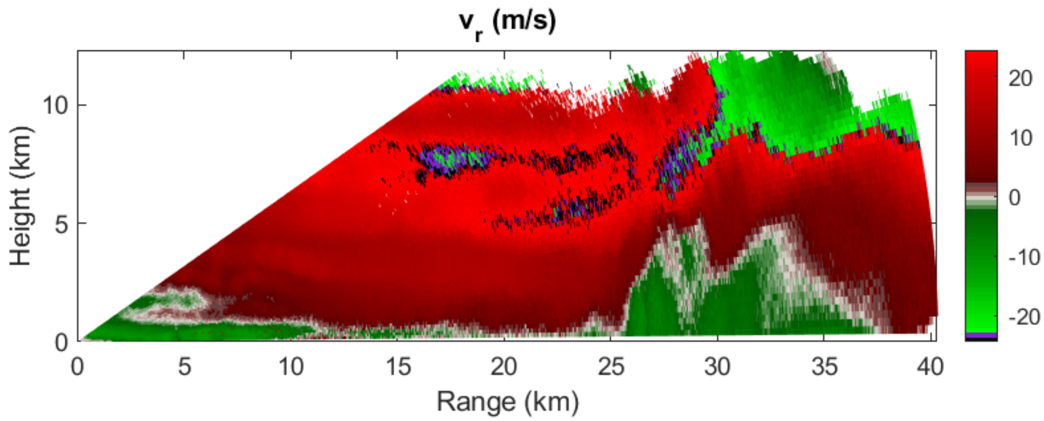

Figure 2.4: A Range Height Indicator (RHI) scan of v_r ($m\,s^{-1}$). The data was collected in Norman, OK, on 4 October 2023 at 22:19:08 UTC using Horus.

unambiguous velocity, which can be calculated using

$$v_a = \frac{\lambda}{4T_s} \tag{2.30}$$

Spectrum width (σ_v) is a measure of the variability of the velocity and is the second moment of the normalized power spectra. There are multiple equations for estimating this moment, with the most common being

$$\sigma_v = \frac{\lambda}{\pi T_s 2\sqrt{2}} \left[ln \left(\frac{\hat{S}}{\hat{R}(T_s)} \right) \right]^{1/2} \tag{2.31}$$

known as the 0,1-lag estimator [2]. Other estimators, such as the 1,2-lag estimator, are also widely used. The 1,2-lag estimator is useful in that it does not require the noise power to be estimated, but its useful range is decreased by a factor of two, so the 0,1-lag estimator is preferred where possible [2]. A plot of σ_v using the 0,1-lag estimator can be found in Figure 2.5.

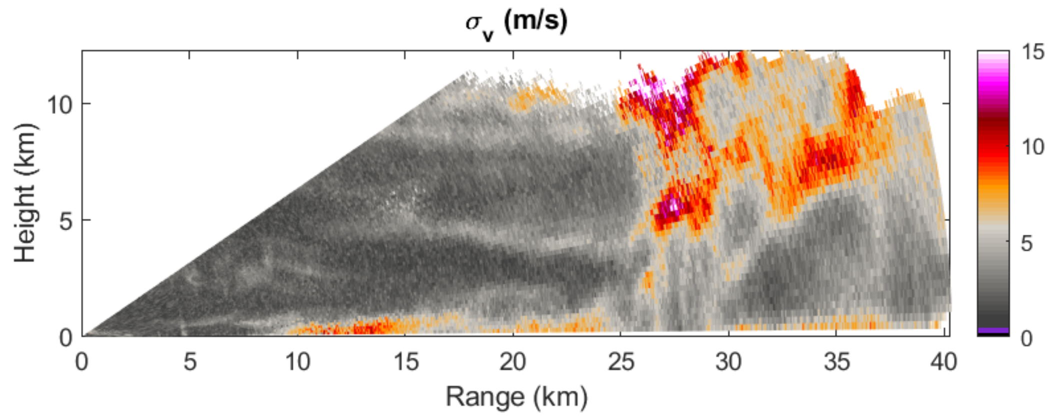

Figure 2.5: A Range Height Indicator (RHI) scan of σ_{v} ($m\,s^{-1}$). The data was collected in Norman, OK, on 4 October 2023 at 22:19:08 UTC using Horus.

2.2.2 Dual Polarimetric Variables

Differential reflectivity (Z_{DR}) measures the difference between the reflectivities in H and V polarization. This can be found using

$$Z_{DR} = 10\log_{10}\left(\frac{\hat{S}_h}{\hat{S}_v}\right) \tag{2.32}$$

For weather, this variable can inform the shape of hydrometeors. Scatterers that are more horizontally aligned will produce a positive Z_{DR}, while scatterers with their major axis in the vertical will produce a negative Z_{DR}. A spherical target with equal power in both polarizations will produce a 0 dB Z_{DR}. A higher Z_{DR} is expected for non-meteorological echoes, typically closer to 6 or 7 dBZ; for hydrometeors, this value typically does not exceed 5 dBZ [17]. A plot of Z_{DR} can be found in Figure 2.6.

The correlation coefficient (ρ_{hv}) is the normalized cross correlation between H and V polarizations, found as follows

$$\rho_{HV} = \frac{|R_{HV}(0)|}{\sqrt{\hat{S}_h\hat{S}_v}} \tag{2.33}$$

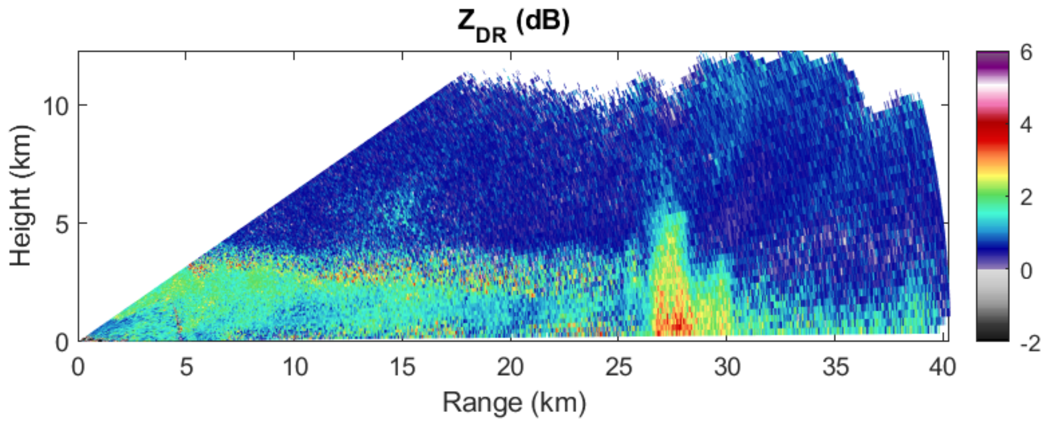

Figure 2.6: A Range Height Indicator (RHI) scan of Z_{DR} (dB). The data was collected in Norman, OK, on 4 October 2023 at 22:19:08 UTC using Horus.

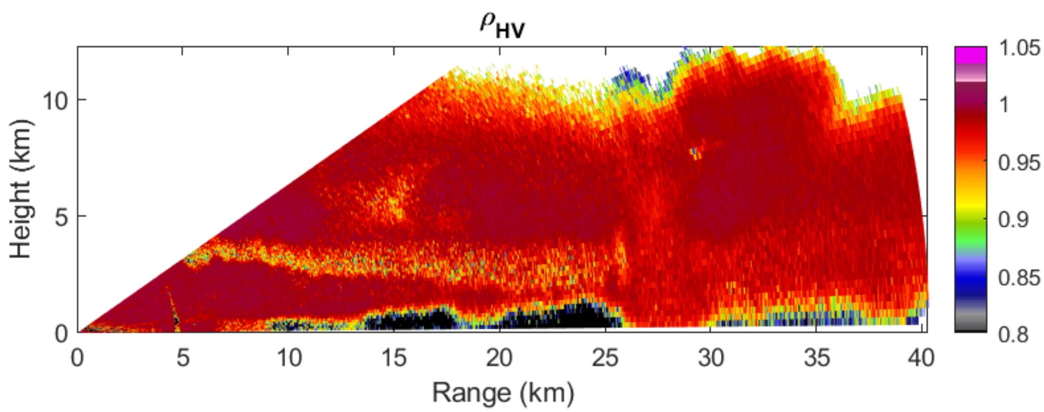

Figure 2.7: A Range Height Indicator (RHI) scan of ρ_{hv}. The data was collected in Norman, OK, on 4 October 2023 at 22:19:08 UTC using Horus.

where $R_{HV}(0)$ is the first lag of the cross correlation estimated at lag 0,

$$R_{HV}(0) = \frac{1}{M} \sum_{m=0}^{M-1} V_h^*(m) V_v(m) \tag{2.34}$$

For hydrometeors, ρ_{hv} is useful to see the difference in height and width, and is usually close to 1. A lower value of ρ_{hv} may indicate mixed precipitation. Non-meteorological targets will also have much lower ρ_{hv}, and are typically expected to be less than 0.8 [17]. A plot of ρ_{hv} can be found in Figure 2.7.

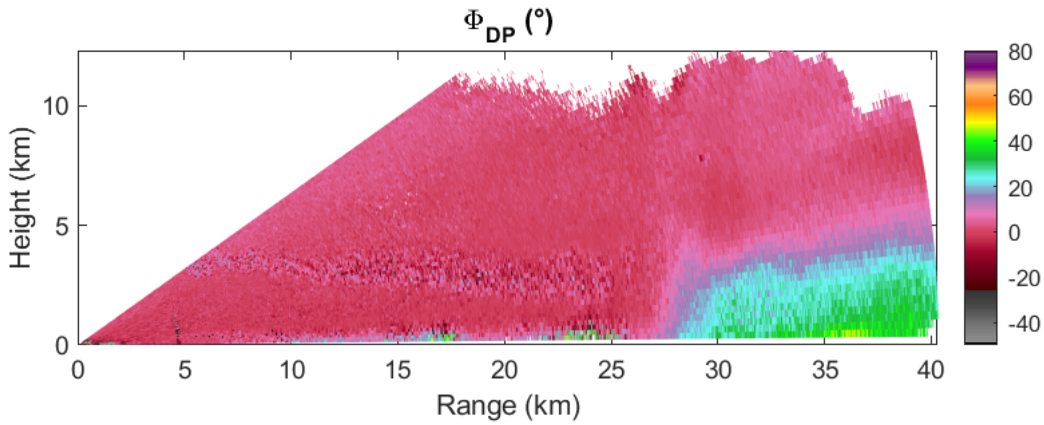

Figure 2.8: A Range Height Indicator (RHI) scan of Φ_{DP} (°). The data was collected in Norman, OK, on 4 October 2023 at 22:19:08 UTC using Horus.

Differential phase (Φ_{DP}) is the phase difference in polarizations expressed in degrees, which can be found using

$$\Phi_{DP} = \angle\left(\hat{R}_{HV}(0)\right)\frac{\pi}{180} \tag{2.35}$$

A plot of Φ_{DP} can be found in Figure 2.8. The phase shifts accumulate with distance, so there is no expected value for this based on the type of echo. However, it is used to calculate specific differential phase, which is used for rainfall rate estimation.

2.3 Summary

This chapter has discussed the signal flow in a typical weather radar system and derived key equations, including the radar equations for point targets and the weather radar equation. The weather variables were also established with their uses and typical values for non-meteorological targets, if applicable. Traditionally, only power is used in detection algorithms, and all the weather variables would be ignored. Understanding what the weather variables would be for a point target is key to utilizing them for a detection algorithm.

The following chapter will establish some vital points about detection of point targets. This will include the derivation of important variables used for detection, issues that arise with various detection algorithms, and specific techniques used. Additionally, the impact of weather clutter on detection of a point target is discussed.

Chapter 3

Radar Detection Techniques

Detection is one of the primary functions of radar, and is used in all applications. For weather detection, the goal is to detect hydrometeors, debris, and various echoes that may indicate severe storms. For other applications, detection is used for point targets; in many instances, this is a type of aircraft. This research will be focusing primarily on the detection of moving point targets – specifically, aircraft – within a storm, and applying known techniques. There are certain things that need to be considered in this instance, including the impact of the weather scattering on the target, how to treat the weather surrounding the point target, and the cost-benefit of incorporating nontraditional variables into a detection algorithm.

3.1 Probability of Detection and Probability of False Alarm

Two main concepts for detection are the probability of detection (P_D) and the probability of false alarm (P_{FA}). These can be defined by

$$P_D = \int_R p(\mathbf{y}|H_1)d\mathbf{y} \tag{3.1a}$$

$$P_{FA} = \int_R p(\mathbf{y}|H_0)d\mathbf{y} \tag{3.1b}$$

with hypothesis H_0 for all observations where it is thought a target is absent, and hypothesis H_1 for all observations where it is thought a target is present in area R. Note that $p(\mathbf{y}|H_1)$ and $p(\mathbf{y}|H_0)$ are the joint probability density functions (PDF) of the signal **y**. The PDFs can be modeled as joint Gaussian distributions

$$p(\mathbf{y}|H_1) = \prod_{n=0}^{N-1} \frac{1}{\sqrt{2\pi\sigma_w^2}} exp\left\{-\frac{1}{2}\left(\frac{y_n - m}{\sigma_w}\right)^2\right\} \tag{3.2a}$$

$$p(\mathbf{y}|H_0) = \prod_{n=0}^{N-1} \frac{1}{\sqrt{2\pi\sigma_w^2}} exp\left\{-\frac{1}{2}\left(\frac{y_n}{\sigma_w}\right)^2\right\} \tag{3.2b}$$

where N is the number of samples, y_n is the n^{th} sample of the signal **y**, m is the mean, and σ_w^2 is the variance of the noise.

Detection requires a threshold to determine an optimal cutoff. In order to determine this threshold, the Neyman-Pearson criterion is used. This criterion is a decision rule which states that P_D can be maximized by setting a threshold for which the P_{FA} does not exceed [18]. This can be determined with a Lagrange multiplier in the form

$$L = P_D + \lambda(P_{FA} - \alpha) \tag{3.3}$$

where α is the threshold that P_{FA} is subject to. Substituting Equations (3.1a) and (3.1b) into Equation (3.3) results in the expression

$$L = \int_R p(\mathbf{y}|H_1)d\mathbf{y} + \lambda\left(\int_R p(\mathbf{y}|H_0)d\mathbf{y} - \alpha\right) \tag{3.4}$$

By setting $P_{FA} = \alpha$, L can be maximized to in turn maximize P_D. The integrals can be maximized by taking the area R to be all the points in the decision space in which $p(\mathbf{y}|H_1) > -\lambda \cdot p(\mathbf{y}|H_0)$ [18]. With this maximization, the decision rule can then be expressed as

$$\frac{p(\mathbf{y}|H_1)}{p(\mathbf{y}|H_0)} \underset{H_0}{\overset{H_1}{\gtrless}} -\lambda \tag{3.5}$$

This is a likelihood ratio test (LRT), which takes hypothesis H_1 if the ratio is greater than $-\lambda$ and hypothesis H_0 if it is not. Taking the natural log of either side gives the log LRT

$$ln\Lambda(\mathbf{y}) \underset{H_0}{\overset{H_1}{\gtrless}} ln(\eta) \tag{3.6}$$

where $\Lambda(\mathbf{y})$ is $\frac{p(\mathbf{y}|H_1)}{p(\mathbf{y}|H_0)}$ and η is $-\lambda$. By substituting Equations (3.2a) and (3.2b) into Equation (3.6), the decision rule becomes

$$\sum_{n=0}^{N-1} y_n \underset{H_0}{\overset{H_1}{\gtrless}} \frac{\sigma_w^2}{m} ln(-\lambda) + \frac{Nm}{2} := T \tag{3.7}$$

where T is defined as the threshold and $\sum y_n$ is a sufficient statistic for the Neyman-Pearson criterion, which can be expressed as $Y(\mathbf{y})$, resulting in the LRT becoming [18]

$$Y(\mathbf{y}) \underset{H_0}{\overset{H_1}{\gtrless}} T \tag{3.8}$$

Now that the sufficient statistic is defined, it is possible to use the LRT to declare a detection if the ratio is greater than this threshold, and assert there is no target otherwise. To determine what the threshold T is, the use of the sufficient statistic Y is required. This is a random variable since it is a function of the random data $\mathbf{y}$, and it takes the form

$Y \sim N(0, N\sigma_w^2)$ [18]. Using this, the expression for P_{FA} becomes [18]

$$\begin{aligned} \alpha = P_{FA} &= \int_T^{+\infty} p_Y(Y|H_0)dY \\ &= \int_T^{+\infty} \frac{1}{\sqrt{2\pi N\sigma_w^2}} exp\left[\frac{-Y^2}{2N\sigma_w^2}\right] dY \end{aligned} \tag{3.9}$$

Evaluating this integral gives

$$\alpha = P_{FA} = \frac{1}{2}\left[1 - erf\left(\frac{T}{2N\sigma_w^2}\right)\right] \tag{3.10}$$

where erf is the error function. Rearranging Equation (3.10), the threshold T can be expressed as

$$T = \sqrt{2N\sigma_w^2} \cdot erf^{-1}(1 - 2P_{FA}) \tag{3.11}$$

Using the same concept from Equation (3.9) and using Equation (3.11), an expression for P_D can be defined as [18]

$$P_D = \int_T^{+\infty} p_Y(Y|H_1)dY = \frac{1}{2}erfc\left\{erfc^{-1}(2P_{FA}) - \frac{\sqrt{N} \cdot m}{\sqrt{2\sigma_w^2}}\right\} \tag{3.12}$$

where $erfc$ is the complementary error function. Here, $(Nm)^2$ is the signal power of the sufficient statistic Y, and the noise power is $N\sigma_w^2$ [18].

With detection, there is always a tradeoff between detection and false alarm rate, which is based on the number of undesired detections. Figures 3.1(a) and 3.1(b) show how a threshold may be chosen based on this tradeoff. In Figure 3.1(a), the false alarm is selected to be $P_{FA} = 10^{-2}$. Then, the threshold is chosen such that it will produce this ideal P_{FA} using Equation (3.11). The P_D will then be equal to approximately 0.244. This is an extremely low P_D, which is due to the poor SNR of 1 dB. The signal power is quite low, so the noise is close to the signal power in this instance. P_D improves with better SNR,

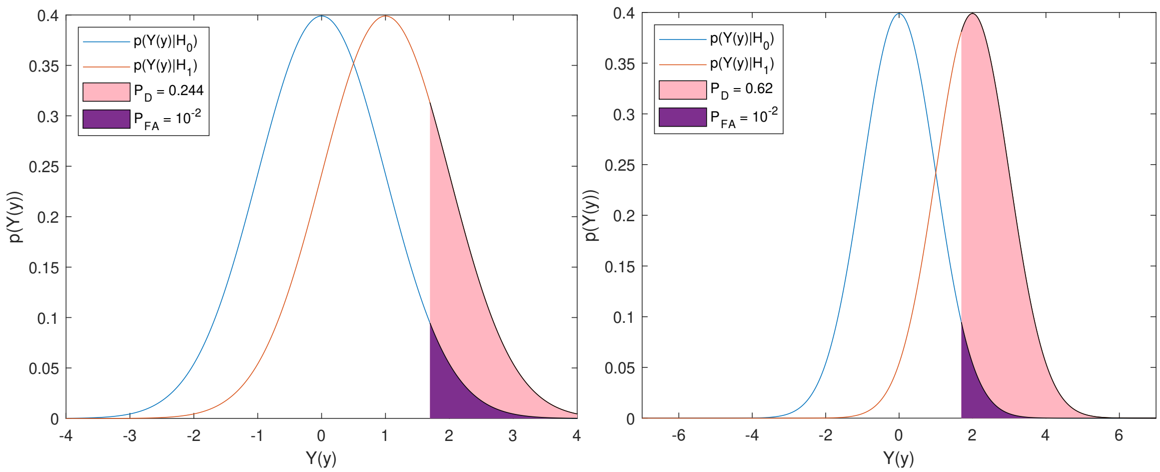

(a) (b)

Figure 3.1: The tradeoff for P_D and P_{FA} in detection for different SNR (dB). The X-axis is $Y(\mathbf{y})$ and the Y-axis is $p(Y(\mathbf{y}))$. The P_D is represented by the red Gaussian distribution, while the P_{FA} is represented by the blue Gaussian distribution. The overlap in false alarms and detections can be seen in the filled in area, with the purple representing false alarms and the pink representing detections. In Figure 3.1(a), the $SNR = 1\,dB$, $P_D = 0.244$, and $P_{FA} = 10^{-2}$. In Figure 3.1(b), the $SNR = 4\,dB$, $P_D = 0.62$, and $P_{FA} = 10^{-2}$.

either through a higher return power, a lowered noise level, or a combination of the two. An improved example can be seen in Figure 3.1(b), with an SNR of 4 dB, P_D of approximately 0.62, and P_{FA} of 10^{-2}. By improving the SNR by a factor of 4, the P_D has been increased by 0.376. From this, it is clear that having a higher SNR is valuable for detection.

3.2 Required SNR Using Shnidman's Equation

Determining the required SNR is helpful in understanding the effectiveness of a detection algorithm. This can be estimated depending on the type of Swerling target via Shnidman's equation [19]. The first step in determining the required SNR is to define a constant η based on the desired P_D and P_{FA} [19]

$$\eta = \sqrt{-0.8ln(4P_{FA}(1-P_{FA}))} + sign(P_D - 0.5) \cdot \sqrt{-0.8ln(4P_D(1-P_D))} \quad (3.13)$$

This constant is then used to determine a constant SNR, which is used in the nonfluctuating target case, or a Swerling 0/V target

$$SNR_{const} = \eta \left(\eta + 2\sqrt{\frac{N}{2} + \alpha - \frac{1}{4}} \right) \tag{3.14}$$

where N is the number of samples and α is 0 for $N < 40$ and $\frac{1}{4}$ for $N \geq 40$ [19]. For fluctuating targets, an approximation for the desired SNR comes from the following

$$(dB)SNR_{approx} = (dB)SNR_{const} + c_{dB} \tag{3.15}$$

where c_{dB} is a constant that changes depending on the desired P_D.

$$\begin{cases} c_{dB} = c_1 & 0.1 \leq P_D \leq 0.872 \\ c_{dB} = c_1 + c_2 & 0.872 < P_D \leq 0.99 \end{cases} \tag{3.16}$$

For these equations, the constants c_1 and c_2 are defined as

$$c_1 = \frac{(((17.7006P_D - 18.4496)P_D + 14.5339)P_D - 3.525)}{K} \tag{3.17a}$$

$$c_2 = \frac{exp(27.31P_D - 25.14)}{K} + (P_D - 0.8)\frac{[0.7log(\frac{10^{-5}}{P_{FA}}) + \frac{2N-20}{80}]}{K} \tag{3.17b}$$

Here, the value K depends on the Swerling type. These values can be found in Table 3.1. Note that there is an accuracy bound for these equations, with an error of less than $\pm 0.5\ dB$ when $0.1 \leq P_D \leq 0.99$, $1 < N < 100$, and $10^{-9} \leq P_{FA} \leq 10^{-3}$ [19].

Table 3.1: K Values for the Shnidman Equation for Different Swerling Cases

Swerling Case	K
I	1
II	N
III	2
IV	2N
V/0	∞

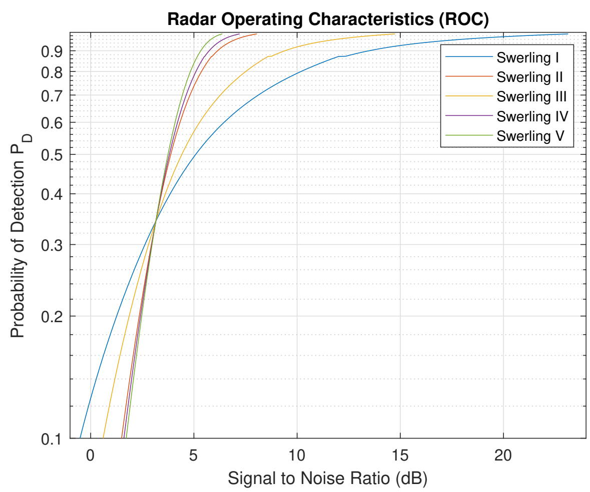

Figure 3.2: Radar Operating Characteristics for various Swerling cases. The $P_{FA} = 10^{-6}$ and $N = 10$. The required SNR (dB) as calculated by Shnidman's equation is the X-axis, and the P_D is the Y-axis.

3.2.1 Radar Operating Characteristics

A way to compare the P_D and P_{FA} using the required SNR is called the radar operating characteristics (ROC). Using Shnidman's equation and a desired P_{FA}, the P_D can be determined. This curve is used to evaluate the effectiveness of a detection algorithm at a given SNR for the various target models. It provides useful information for the expected P_D given the number of pulses and ideal P_{FA}. If the SNR is known, the ROC can be used to determine the best possible P_{FA} to be used. Figure 3.2 shows the ROC of all Swerling model types for a chosen P_{FA} of 10^{-6} and $N = 10$.

3.3 Constant False Alarm Rate

The Constant False Alarm Rate (CFAR) is a common type of algorithm used for detection in radar. As stated in the derivation for Equation (3.8), the P_D can be maximized by setting a P_{FA}. CFAR algorithms use this fact to their advantage by setting an optimal P_{FA}, taking a target cell in the data, and examining the cells in a given range around it to determine if there is a potential target in the cell or not. What differs across various CFAR algorithms is the way the threshold factor in Equation (3.8) is determined. Note that the threshold established in Equation (3.11) and the P_{FA} established in Equation (3.10) depend on the variance of the interference power (σ_w^2); to exhibit CFAR behavior, the P_{FA} cannot depend on the interference power. Interference power may not be known, but will be estimated with various techniques. The required threshold then can be estimated by

$$\widehat{T} = \alpha \cdot \widehat{\sigma_w^2} \tag{3.18}$$

where α is a threshold multiplier determined by [18]

$$\alpha = M \left[P_{FA}^{-1/M} - 1 \right] \tag{3.19}$$

Here, M is the number of cells used in the training band, and the P_{FA} is the desired P_{FA}.

To perform CFAR, a cell under test (CUT) is taken, with a surrounding guard band and training band. The guard band acts as a barrier to keep the information of the potential target from altering the threshold and is ignored when estimating a threshold. This is important in the event that the target RCS is larger than the size of the cell being examined, as the higher power of the target would be present in a surrounding cell and potentially cause a missed detection without the guard band. The training band is made of the remaining cells in the surrounding area which are kept and used to determine the threshold. A visualization

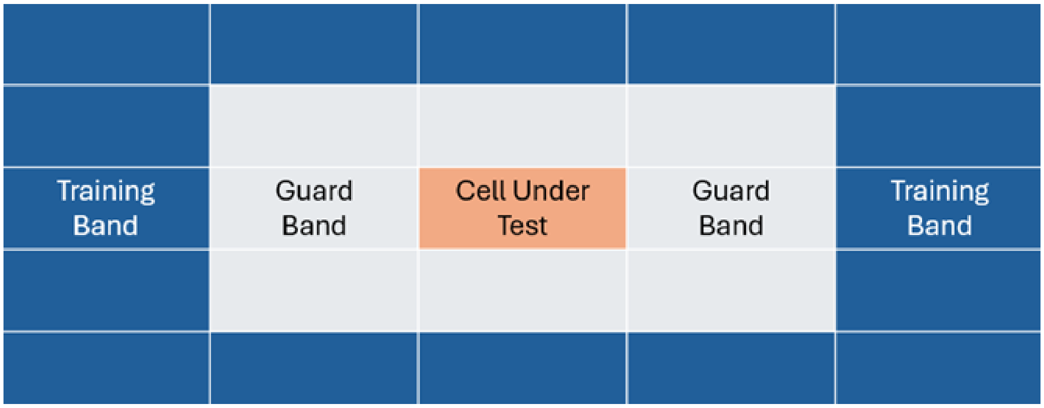

Figure 3.3: Illustration of a 2D CFAR cut, including the training band (blue), the guard band (white), and the CUT (orange). The guard band is ignored and the training band is used in threshold estimation.

of the CUT and bands can be seen in Figure 3.3.

3.3.1 Various CFAR Algorithms

As mentioned in Section 3.3, there are multiple ways to perform a CFAR algorithm, which differ by the way that the threshold is determined. One of the requirements for CFAR is the set P_{FA}, which is done by multiplying the calculated threshold by the constant α defined in Equation (3.19). For an improved P_{FA}, α will become larger and thus inflate the threshold.

Of the various CFAR algorithms, one of the most common is Cell-Averaging CFAR (CA-CFAR) [20]. The average of the cells in the training band is used for the threshold, determined by

$$T = \alpha P_n \tag{3.20}$$

where α is the constant defined by Equation (3.19), and P_n is the computed average of the cells in the training band. The typical use of this technique is when only one target is present, or targets are significantly spread across the area. With no target or clutter present in the training band, this average is expected to be the noise power of the signal, providing

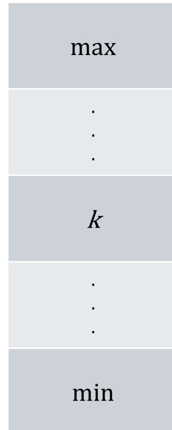

Figure 3.4: Visualization of the ordered data for the OS-CFAR algorithm, with the k^{th} value selected. The training band is sorted into a column vector to determine the threshold.

clean results for detection.

In the case of multiple targets, they may interfere with each other and cause more false alarms than desired. In the presence of strong clutter such as weather, it becomes significantly harder for this algorithm to detect targets, as higher power areas of weather may cause numerous false targets to appear and render results useless. In this case, another algorithm will prove more useful.

In a multiple target case, the Ordered-Statistics CFAR (OS-CFAR) algorithm is often used. This technique takes the training band and sorts it, using the k^{th} element to determine a threshold value [21]:

$$T = \alpha X_{(k)} \tag{3.21}$$

This can be done in multiple dimensions, and for the purposes of this work, a 2D-OS-CFAR will be used [22]. This looks in both range and elevation or azimuth depending on the scanning type. Although the guard and training band are taken in two dimensions, the training band is sorted into a column vector in order to determine the threshold, as seen in Figure 3.4. It is typical for the k^{th} value to be selected as $3M/4$, where M is the number of cells in the training band.

This version of CFAR is particularly useful when there are multiple targets present, or when there is the presence of larger amounts of clutter where the average may be skewed. With a target present in weather clutter, this algorithm outperforms the CA-CFAR algorithm as OS-CFAR is better geared towards locating outliers in the data regardless of the surrounding power.

A more recent algorithm for CFAR based on the interquartile range (IQR-CFAR) has been proposed by [23]. Using this algorithm, two thresholds are determined in order to find outliers on either end of the data. The thresholds are determined by

$$T_{r_1} = Q_1 - \alpha_{r_1} \cdot IQR \tag{3.22a}$$

$$T_{r_2} = Q_3 - \alpha_{r_2} \cdot IQR \tag{3.22b}$$

where Q_1 is the first quartile, Q_3 is the third quartile, $IQR = Q_3 - Q_1$ is the interquartile range (IQR), and α_{r_1} and α_{r_2} are the scale factors to produce the desired thresholds computed from Equation (3.19), although α_{r_2} will be the negative of the result as it is setting the threshold in the opposite direction of a traditional CFAR algorithm.

While this algorithm is not applicable to traditional detection algorithms utilizing power, it is useful for detecting outliers in variables such as v_r, which can be positive or negative, and which should be different for a target versus the surrounding area. In other words, this two-sided approach is useful for when the target is expected to be different from the data, but it is uncertain whether it will be larger or smaller than the area around it.

Similar to OS-CFAR, the IQR and respective quartiles are computed by taking the training band and converting it to a column vector for two dimensional data, as seen in Figure 3.5.

Figure 3.5: Visualization of the ordered data for an IQR-CFAR algorithm, with the threshold values highlighted. The training band is sorted into a column vector to determine the threshold.

3.4 Impact of Clutter on Detection of a Point Target

In detection, clutter is the presence of any unwanted signal. For weather radar, clutter may be birds, aircraft, buildings, smoke, or other non-meteorological echoes. For point target detection, the desired signal comes from aircraft and weather joins the list of clutter. Stationary clutter such as buildings may be filtered out, but the presence of weather clutter provides complications for point target detection. Weather clutter will be heavily spread out across the area and likely to interfere with the signal of the target. There are two possibilities when weather and a target are present: the target is located inside the storm, or the target is located in clear air. Depending on the scenario, different algorithms may perform better.

To analyze where there is both weather clutter and a point target, the power spectral density (PSD) is a useful tool. This is the distribution of power as a function of frequency, and can be computed a number of ways. The PSD estimator used in this thesis is called the periodogram spectral estimator, and can be defined as [24]

$$PSD = \frac{1}{N}\left|\sum_{n=0}^{N-1}(y(t)e^{-j\omega n})\right|^2 \tag{3.23}$$

where $y(t)$ is a finite signal of N samples which is passed through a window function. In this thesis, the Hamming window is used, which is defined by

$$w(n) = 0.54 - 0.46cos\left\{\frac{2\pi n}{N_{win}-1}\right\}, 0 \leq n \leq N_{win}-1 \tag{3.24}$$

where N_{win} is the window length. The PSD is the discrete Fourier transform (DFT) of the windowed IQ samples over the window length. The frequency spectrum can be expressed in $m\,s^{-1}$ to see the velocities at which the data are concentrated.

The velocity of the target and the weather are expected to be different, causing two separate peaks in the PSD. This can be seen in Figure 3.6(a). In this example, the target has a peak velocity at -25.7517 $m\,s^{-1}$ while the weather has a peak at 3.86276 $m\,s^{-1}$. Since the calculated v_{r} is a weighted average, the calculated v_{r} at this point comes out to be -25.1406 $m\,s^{-1}$. Since the target has such a strong return and the SNR here is also high, the calculated v_{r} is close to that of the target. With worse SNR or a weaker target, this result may be closer to the weather. Another example of this is found in Figure 3.6(b). Here, the target is seen with a peak velocity at -22.6615 $m\,s^{-1}$ and the weather with a peak at 1.80262 $m\,s^{-1}$, but the return power for the weather is stronger than that of the target. The calculated v_{r} at this point comes out to be -1.8756 $m\,s^{-1}$, which is different than that of the storm, but much farther away from the velocity of the target seen in the PSD.

Additionally, looking at the PSD, the power of the target versus the power of the storm can be seen. In Figure 3.6(a), the power of the target is much higher than that of the storm,

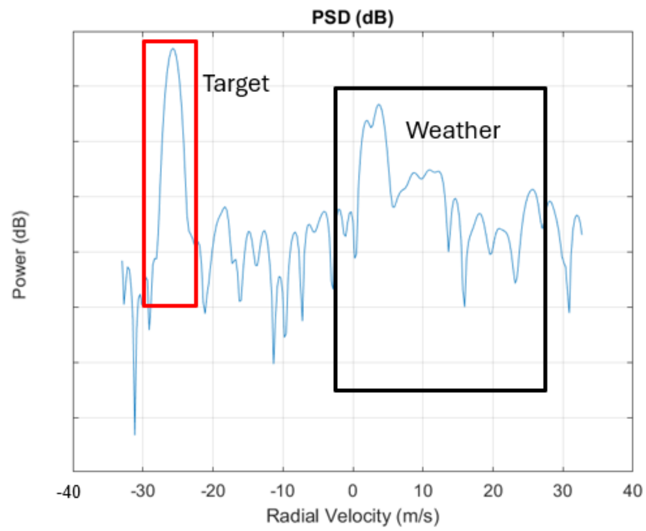

(a)

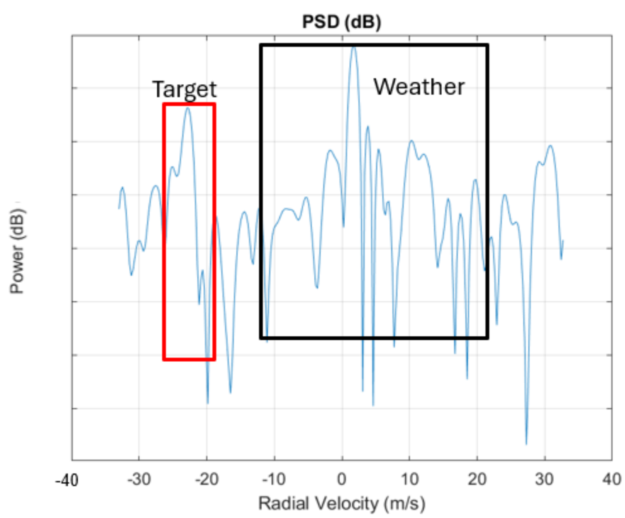

(b)

Figure 3.6: The Power Spectral Density (PSD) of a point target in weather. The X-axis is the v_{r} of the spectrum ($m\,s^{-1}$), and the Y-axis is the signal power (dB). The PSD corresponds to the returns from the V channel. Figure 3.6(a) shows a strong point target in weather. The target has a peak at $-25.7517\ m\,s^{-1}$, while the weather has a peak at $3.86276\ m\,s^{-1}$. Figure 3.6(b) shows a weak point target in weather. The target has a peak at $-22.6615\ m\,s^{-1}$, while the weather has a peak at $1.80262\ m\,s^{-1}$.

and should be easily identifiable by a traditional CFAR algorithm. However, the target in Figure 3.6(b) is lower than that of the weather. This indicates that the surrounding power is likely a similar level as that of the weather, meaning the power of the target will go undetected. Without a filter to remove the weather clutter, traditional CFAR algorithms using power will not work for this target.

In clear air, detecting a target may be relatively simple, as the return power will be much higher where a point target is located as opposed to where there is nothing. However, in the presence of weather clutter, it can be seen that certain issues will arise. It is possible that the target and the weather have similar return powers, as seen in Figure 3.6(b), hindering CFAR techniques. In this instance, a weather-aware CFAR algorithm utilizing additional variables may improve the detection rate while maintaining valuable information for meteorologists.

3.5 Summary

This chapter has established key concepts in detection, including P_D, P_{FA}, and required SNR. Additionally, various CFAR algorithms and their respective uses have been discussed. Finally, the impact of weather clutter on a point target has been demonstrated, showing when a variable besides power may be useful in a CFAR algorithm.

Now that background for the weather variables and various detection algorithms have been established, a new algorithm for detection involving the variables and techniques presented will be used. The data used with this algorithm, along with the process of it, including techniques used prior to running the algorithm to help minimize false alarms, will be described.

Chapter 4

Weather-Aware CFAR

Various CFAR algorithms have been proven to work well in various situations, such as clear air, multiple targets, or along a clutter edge. However, CFAR techniques have drawbacks when it comes to observing targets inside significant clutter, such as weather. As previously mentioned, CA-CFAR is not an ideal solution, and although OS-CFAR performs significantly better, using only the power to detect point targets poses a challenge where the clutter may be the same signal power as the target or even stronger. In order to detect harder to find targets while keeping a lower level of false alarms, combining a variety of CFAR algorithms exploiting the new information provided by weather radar variables is proposed.

4.1 Experimental Configuration

The data used in this research are V polarization, plan position indicator (PPI) and were collected on 26 January 2024, from 22:22:46 to 22:47:58 UTC using the Horus radar. These data were part of an experiment conducted by the ARRC for the Defense Advanced Research Projects Agency (DARPA) Beyond Linear Processing (BLiP) project involving a Phoenix Air Learjet 36A aircraft and ground emitter. The BLiP program aims to improve radar performance via advanced, non-linear signal processing techniques [25]. The premise

Figure 4.1: The profile prepared for the S-curve test, from [26]

of the project is that non-linear signal processing techniques are required in more complex and realistic environments. The success of BLiP would enable radar systems to become smaller and less expensive without losing capability [26].

There were five separate profiles designed for this experiment, the fifth of which is used in this work. This profile can be found in Figure 4.1, and involves an S turn maneuver of the Learjet 36A. During the experiment, the aircraft maintained a constant indicated airspeed of 220 knots with an altitude range from 2,750 feet to 16,850 feet above mean sea level (MSL) [26]. The deployment location can be found in Figure 4.2.

For the experiment, three different array configurations were used with the five profiles, with a total of fifteen trials. The scan design for the radar used in this thesis included a single PRT at 100% of the array scale. This array configuration can be found in Figure 4.3. Additional information on the specifications of the configuration can be found in Table 4.1. The scan covered $-45°$ to $45°$ in azimuth and $0°$ to $20°$ in elevation. For this thesis, only the elevation at $3.125°$ is used, with all azimuth angles used. A total of 499 volume scans were collected during this time. There was light precipitation and multiple aircraft were

Figure 4.2: The deployment location of the Horus radar during the experiment, courtesy of David Schvartzman.

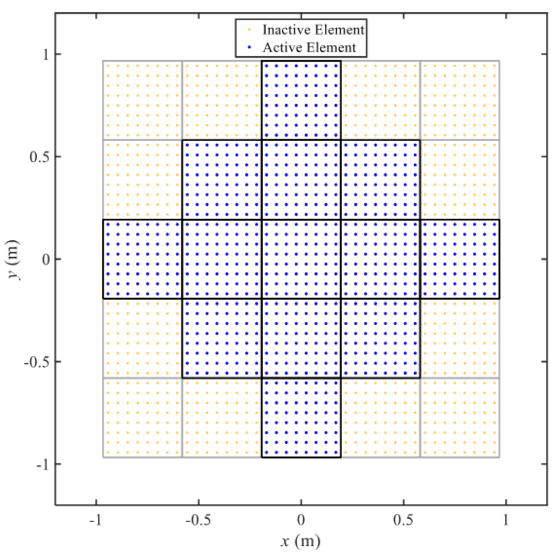

Figure 4.3: The array configuration for the data at 100% scale, courtesy of David Schvartzman.

Table 4.1: Specifications for the Array Configuration

PRF	1.35 kHz
Rx Bandwidth	3.90625 MHz
Range Swath	5-95 km
Array Scale	100%
Subarray Panels	13
Total data rate	$\sim$ 1.5 Gbps
Peak Power	8.32 kW per polarization
Frequency	3.070 GHz
Beamwidth	3.3° az/el

captured in the data. In addition to the multiple aircraft, the data also includes "simulated targets," which will be described in the next section. These targets demonstrate the various possible outcomes with weather clutter and a point target, including weak and strong targets in weather clutter and in clear air. There are both singular target and multiple target cases.

4.1.1 Target Simulation

A "target simulator" is a device that can receive a radar's pulse, delay and modulated the pulse, and return the signals. Such a device was deployed on the Learjet 36A to provide simulated targets during a portion of the data. These targets can have a programmed power level and Doppler velocity, but can only be delayed. This causes what appears to be a row of targets in one azimuth beam, as shown in Figure 4.4. The initial target at $48\,km$ is the Learjet 36A, followed by the simulated, time-delayed targets. This is done by receiving the transmitted pulse from the radar and digitally delaying the signal. The targets are also scaled for varied effective RCS [26]. This causes the variability in how the targets appear in the Doppler map, with some appearing much stronger and having more spread in the velocity axis. Once the signal is scaled and delayed, it is transmitted back towards the radar.

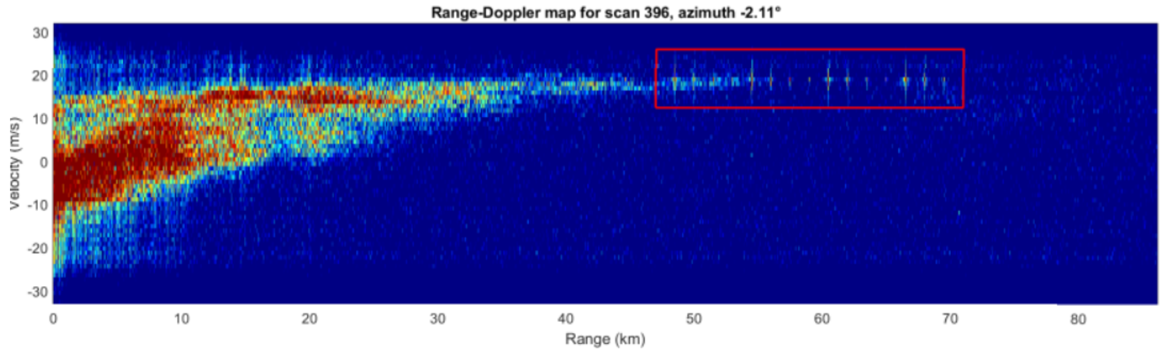

Figure 4.4: The range Doppler map showing the real target followed by simulated targets. This map is for the azimuth beam at $-2.11°$. The target located at approximately $48\,km$ is the real target, followed by the time delayed simulated targets. This scan was taken at 22:42:45 UTC.

4.1.2 Digital Beamforming

Digital beamforming is a concept which allows for rapid and precise control of the radar beam. The phase and amplitude of signals are adjusted digitally to steer the beam without physically moving the antenna. With analog beamforming, the phase and amplitude of signals are adjusted using components such as phase shifters and attenuators, with the direction of beam propagation steered by physically pointing the radar antenna in the desired direction. Analog beamforming also only allows for one beam at a time. With digital beamforming, the phase and amplitude adjustments are performed digitally with computational algorithms, which can be used for transmitting and also for postprocessing in receive. The software-controlled beamforming allows for more flexible, complex, and precise control over beamforming, as well as for the transmission and reception of multiple beams simultaneously. Digital beamforming greatly improves the temporal resolution, and the spatial resolution can be improved with pulse compression [1].

4.1.3 Pulse Compression

Pulse compression is a technique in which a wide pulse is sent to achieve a large radiated energy, which gives a higher sensitivity, and processed to a narrow pulse using a matched filter in order to achieve better range resolution. For unmodulated pulses, range resolution is dependent upon the pulse width τ_s and improves with shorter widths, and can be defined as

$$\Delta r = \frac{c\tau_s}{2} = \frac{c}{2\beta} \tag{4.1}$$

where β is the bandwidth and the pulse width $\tau_s = 1/\beta$. If a modulated pulse is sent out, range resolution is dependent only on the bandwidth β of the transmitted pulse, not the pulse width τ_s. It is typical that a modulated pulse will be used in weather radar.

A matched filter is the linear filter which maximizes the output SNR, and is the convolution of the IQ signals with the time reversed transmit waveform. The spectral transfer function of the matched filter is expressed as [27]

$$H_{MF}(\omega) = \frac{2k}{N_0} S_i^*(\omega) e^{-j\omega t} \tag{4.2}$$

where $\frac{N_0}{2}$ is the noise spectral density (watts/Hz), k is a constant, and $S_i(\omega)$ is the transmit waveform.

4.1.4 Horus Beamforming Strategy

The data used in this thesis were created using 64 primary transmit beams per raster with one receive beam per digital subarray seen in Figure 4.3, totaling thirteen receive channels for digital beamforming. Additionally, there were 64 pulses per coherent processing interval (CPI). A 2.5x spoiled beam on transmit was used to illuminate a broad area, while a pencil beam used on receive regained spatial selectivity. The patterns used for the spoiled

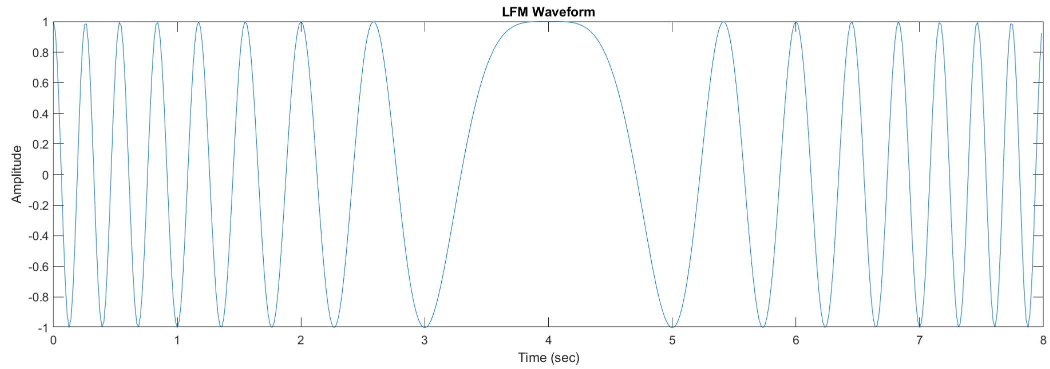

Figure 4.5: A linear frequency modulated (LFM) waveform with a pulse width of $8\mu s$ and a bandwidth of 8 MHz.

transmit beams minimize ripple across the mainlobe at the cost of increased sidelobe levels, giving a peak sidelobe level at approximately -7.5 dB and a ripple of 0.22 dB. The loss is approximately 10.2 dB, with an absolute transmit gain of 24.11 dB. An untapered linear frequency modulated (LFM) waveform was used for pulse compression. An LFM is a sinusoidal wave which increases in frequency linearly over time. This waveform is expressed as

$$x(t) = exp\left(j\pi\frac{\beta}{\tau_s}t^2\right) \tag{4.3}$$

where β is the bandwidth and τ_s is the pulse width. An example of this waveform can be seen in Figure 4.5.

4.2 Ground Clutter Mitigation

An important consideration for detection is the mitigation of ground clutter. Ground clutter is the presence of unwanted returns which come from stationary objects on the ground such as buildings, trees, and other objects near the radar. In detection, this clutter can appear as a target due to the stronger return power. Additionally, in the presence of weather clutter, they will also have a different velocity since they are stationary. This may also provide a false alarm if detecting with v_{r}. There are many ways to filter out this clutter. The technique employed in many weather radars is the Gaussian model adaptive processing in the time domain (GMAP-TD) [28]. Using this filtering technique, a clutter width is first set. This is done by determining the wind speed of the data. The wind speed is plugged into [2]

$$\sigma_c = \frac{0.008 v_w^{1.2}}{2\sqrt{2ln(2)}} \tag{4.4}$$

where v_w is the wind speed mentioned above. Additional clutter width may come from the rotation rate of the antenna [2]. As the radar used for these data is phased array, there is no rotation rate for which to account, and accounting for the wind speed is enough. This can then be used to determine the auto-covariance of the clutter, defined as [28]

$$\boldsymbol{R_c}(\tau) = P_c \; exp\left(-\frac{8\pi^2\sigma_c^2\tau^2}{\lambda^2}\right) \tag{4.5}$$

where τ is the time variable, P_c is the clutter power, and λ is the wavelength. With the auto-covariance matrix determined, the clutter filter matrix **A** is designed as [28]

$$\mathbf{A} = \left(\frac{\boldsymbol{R_c}(\tau)}{P_n} + \boldsymbol{I_m}\right)^{-1/2} \tag{4.6}$$

where P_n is the noise power and $\boldsymbol{I_m}$ is the identity matrix. The IQ signal is then multiplied by the filter matrix and the clutter is filtered. Figures 4.6(a) and 4.6(b) show the PSD of ground clutter before and after the filter is applied.

To ensure that the filter is properly working and only removing ground clutter, additional figures are shown. Figures 4.7(a) and 4.7(b) show the PSD where a known target is located, and from this it is clear that only the few samples around 0 $m\,s^{-1}$ are affected by the filter, with the rest of the spectrum remaining the same. This can also be seen in Figures 4.8(a) and 4.8(b), which show a weather spectra that is found near 0 $m\,s^{-1}$. The end which is near to 0 $m\,s^{-1}$ is slightly affected, but the overall spectrum remains the same, and the

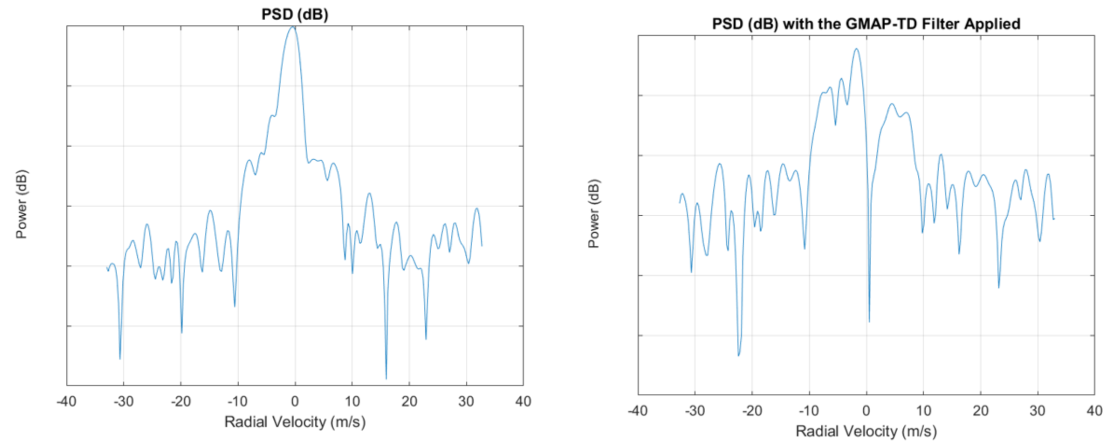

(a) (b)

Figure 4.6: The PSD of a ground clutter, located close to the radar. The X-axis is the v_r of the spectrum ($m\,s^{-1}$), and the Y-axis is the signal power (dB). The PSD corresponds to the returns from the V channel. Figure 4.6(a) shows the spectrum prior to GMAP-TD filtering, and Figure 4.6(b) shows the spectrum after the filter is applied.

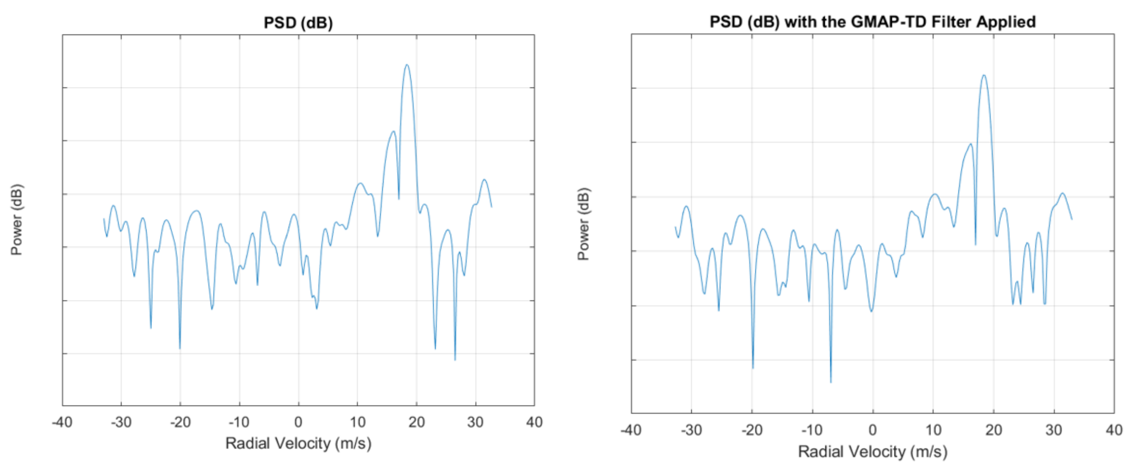

(a) (b)

Figure 4.7: The PSD of a target, located at the edge of the storm. The X-axis is the v_r of the spectrum ($m\,s^{-1}$), and the Y-axis is the signal power (dB). The PSD corresponds to the returns from the V channel. Figure 4.7(a) shows the spectrum prior to GMAP-TD filtering, and Figure 4.7(b) shows the spectrum after the filter is applied.

shape of the weather is still distinct and visible.

With the ground clutter filtered, it is now possible to employ a detection algorithm with

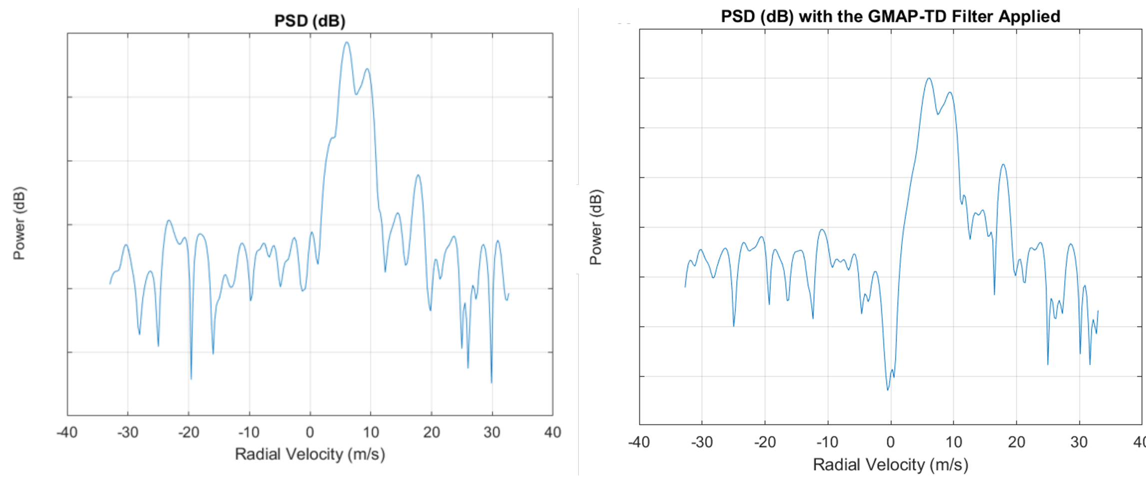

(a) (b)

Figure 4.8: The PSD of weather. The X-axis is the v_r of the spectrum ($m\,s^{-1}$), and the Y-axis is the signal power (dB). The PSD corresponds to the returns from the V channel. Figure 4.8(a) shows the spectrum prior to GMAP-TD filtering, and Figure 4.8(b) shows the spectrum after the filter is applied.

fewer false alarms. The algorithms used in this thesis will be explained in the next section.

4.3 Single-Variable CFAR Algorithms

In order to determine the best combination of weather variables for a detection algorithm, algorithms for each individual variable must first be established. The algorithms in this thesis utilize Z_v rather than power as a typical detection algorithm would use, since Z_v is a range calibrated power. The two variables would be comparable in performance regardless of which was chosen. An OS-CFAR algorithm was used for Z_v, with the k^{th} value chosen as $3M/4$ and the α constant as described in Equation (3.19).

To incorporate a CFAR algorithm using σ_v, it is important to note that a target's σ_v will likely vary from that of the surrounding weather, but may be larger or smaller. With this in mind, IQR-CFAR was implemented [23]. The same idea applies for v_r, as both the storm and target can change direction, allowing for positive or negative values in either. A

Table 4.2: Specifications for the CFAR Bands

Variable	Desired	Corresponding Number of Cells
Guard Azimuth	1.5°	1
Training Azimuth	2.5°	2
Guard Range	40 m	1
Training Range	360 m	9

target should be a different velocity from the area of the storm it is found in, and therefore rather than using a traditional CFAR method, the IQR-CFAR method used for σ_{v} was also implemented here. Regardless of the direction of the weather or target, the target should be an outlier on one end of the sorted data. Note that since the data used in this research are single polarization, only these three variables will be used.

Rather than setting a specific number of cells for the guard and training bands, a desired range (m) and azimuth ($^\circ$) are used to calculate the corresponding number of cells to be included. The chosen values and the corresponding number of cells can be found in Table 4.2. This approach is taken so that an approximately equal area can be used regardless of the beam width or size of the range gate. This decision comes from the idea that weather radar typically use larger range gates than a radar operating solely for detection. It is a larger area than would typically be used for a detection algorithm, but ensures that there is enough data in the training band for an effective CFAR algorithm. The range gates of the data used are approximately $38.4\ m$, and the azimuth beams are approximately 1.4°. With established guard and training bands, a desired P_{FA} can be chosen and the single variable algorithms are ready to be used.

4.4 A Proposed Weather-Aware CFAR Detection Algorithm

Now that the single variable algorithms are established, it is possible to combine the variables to create an improved detection algorithm, established as the Weather-Aware CFAR (Wx-CFAR) algorithm. To create an optimal algorithm, a few considerations arose from findings with the single variable CFAR algorithms and from established knowledge of CFAR performance. The first consideration is how to combine the variables in the event that there is weather clutter. Rather than performing the CFAR algorithm for each variable on every CUT and declaring a detection if all three variables detect it, a different approach was taken. The algorithm begins with the best performing variable, which was determined by the number of targets detected in various scenarios using the single variable algorithms. If this variable has a detection, then CFAR is performed on the CUT using the additional variables. If those variables also provide a detection, the 'confidence' of the algorithm is improved.

The idea for a confidence-based CFAR was inspired by the use of various probability models for different circumstances in [29] and the use of a decision tree to increase detection accuracy in [30]. The confidence of the algorithm for a detection may only be improved; there is no penalty incurred if any variable does not detect a target, as a target may present similarly to the meteorological echoes. Consider the case in which σ_{v} of the storm is narrow, but the point target also has a narrow σ_{v}. There may be detections in power and v_{r}, but not in σ_{v}. Rather than penalizing the algorithm for not detecting in every variable, it simply remains at a lower confidence.

The next consideration is that traditional, power-based CFAR already works well in clear air. The return signal of clear air will remain close to the noise level, which provides inaccurate calculations for variables like v_{r}. In weather radar, the variables are censored when there is extremely low SNR to avoid noisy returns. An example of censoring can be

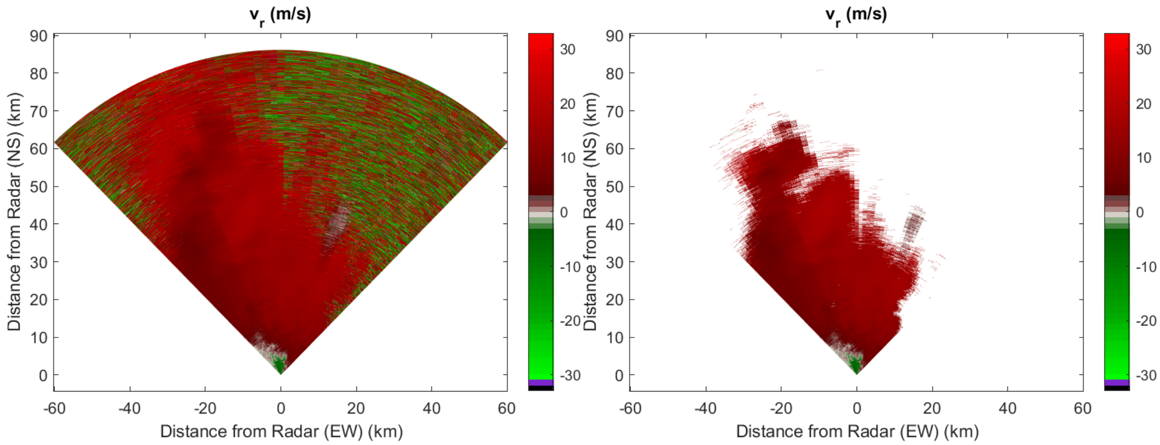

(a) (b)

Figure 4.9: The v_r of a volume before and after censoring is applied. Figure 4.9(a) shows the calculations without censoring applied. In clear air, the v_r becomes extremely noisy. Figure 4.9(b) shows v_r after censoring, where only the storm is visible.

seen in Figures 4.9(a) and 4.9(b). With censoring applied, it may be difficult to determine whether a CUT is a target in clear air or the edge of the weather clutter. Additionally, if a target is found in the clear air of the volume, it should be easily detectable without false alarms using only the Z_v with a traditional CFAR algorithm. Furthermore, the σ_v in clear air should be significantly wider than that of a target. Thus, if the multi-variable algorithm detects clear air, only Z_v and σ_v will be used for that CUT.

After determining whether the CUT is in clear air or weather clutter, the next consideration is with which variable to begin detection. In clear air, the return power of the target will be much higher than that of the air, making Z_v a good candidate to check first in this situation. If a detection in Z_v occurs, then σ_v will also be used for that CUT in clear air. However, weather clutter may have a high return power and provide a similar power level to a potential target, meaning that Z_v may miss detections. A higher number of false alarms may also appear if the weather has more condensed areas of higher precipitation, appearing like a target. With v_r, it is more likely to find a target in the clutter, as the weather clutter will typically have a more uniform v_r in a given area which is likely to differ from that of

Table 4.3: Determined Weights for Each Weather Variable in the Weather-Aware CFAR Algorithm

Variable	Clutter Presence	Weight
Z_{v}	Clear air	2.5
v_{r}	Clear air	-
σ_{v}	Clear air	1.25
Z_{v}	Weather clutter	1
v_{r}	Weather clutter	1.5
σ_{v}	Weather clutter	1.25

the point target. Therefore, if the CUT is located in weather clutter, the first variable to be checked will be v_{r}. If it provides a detection, the CFAR algorithms for σ_{v} and Z_{v} will then be used and confidence adjusted accordingly. Results demonstrating this claim for v_{r} will be shown in Chapter 5.

Another consideration is by how much to improve the confidence for each detection. In a typical CFAR algorithm, the detection for the CUT will either be returned as 0 for no detection or 1 for a detection. However, the use of confidence could extend the returned value above 1 for detections. Weights for each variable were determined based on how well they performed with known targets. The performance was evaluated based on the detection of various types of targets. The false alarm rate that each variable's algorithm produced with the clutter present was also considered. Further details on why these weights were chosen will be discussed in Chapter 5 when target detection and false alarm rate are presented. The weights for each variable can be found in Table 4.3. Note that since the detection algorithm does not incorporate v_{r} in clear air, the selected weights differ depending on the presence of clutter so that a detection at full confidence remains the same in both clear air and weather clutter.

With weights determined for both scenarios considered, the weather aware CFAR al-

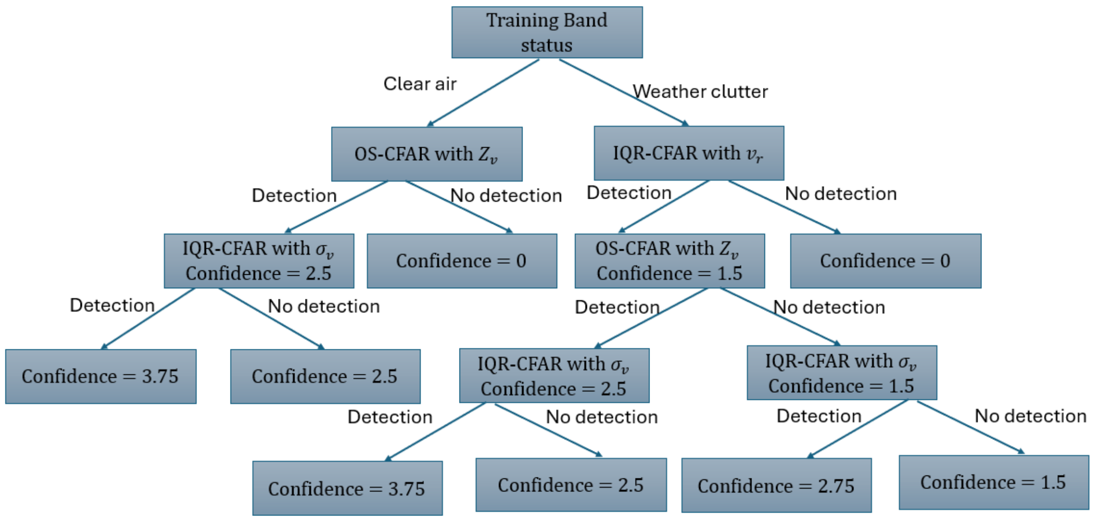

Figure 4.10: The decision tree for a CUT of the weather aware CFAR algorithm. Each possible confidence outcome is depicted for both clear air and weather clutter, ranging from Confidence $= 0$ to Confidence $= 3.75$.

gorithm is now fully described. The decision tree for this algorithm can be seen in Figure 4.10. This depicts each possible outcome for both clear air and weather clutter, and the various combinations of confidence.

4.5 Summary

The data used in this thesis include multiple point targets and light precipitation. It uses digital beamforming and pulse compression via matched filtering for improved temporal and spatial resolution. Prior to performing detection, the implementation of ground clutter mitigation is useful in removing clutter which may present as potential false alarms while maintaining the integrity of the weather and point target signals. Then, single variable CFAR detection algorithms may be implemented to determine how well each weather variable performs individually. Descriptions of each of the individual algorithms are provided, along with the specifics of how the guard and training bands were determined. Once the single variable CFAR algorithms are established, an improved weather aware CFAR detection algorithm is proposed. This algorithm accounts for whether the CUT is located in clear air or weather clutter, which determines which variables to use. The algorithm also implements weights for each variable depending on which most frequently detects point targets in various scenarios.

The next chapter will analyze the performance of the Wx-CFAR algorithm. In order to do this, the false alarm rate of the individual CFAR algorithms and of the Wx-CFAR algorithm are determined. Additionally, various scenarios involving point targets and weather clutter are identified, and the ability of the algorithm to detect the targets is assessed.

Chapter 5

Analysis of the Performance of the Weather-Aware CFAR Algorithm

In order to assess the effectiveness of the Wx-CFAR algorithm, various real target scenarios in the data were determined. The various target cases include: a single target in weather clutter, a single target in clear air, multiple targets in weather clutter, and multiple targets in clear air. In addition, the targets located in weather clutter may have a stronger return power than the precipitation, or may be weaker. Furthermore, a case of a target going at similar v_{r} to the weather was identified. Easier to identify targets are found in clear air or have a much stronger signal strength than the weather clutter surrounding it. In order to determine the effectiveness of the algorithm, targets in each of these scenarios must be located.

5.1 Identification of Representative Targets

In order to identify targets, a few methods were employed. First, the azimuth angle was identified using PPI plots of the various weather variables. Targets located in weather clutter were easier to identify using v_{r} plots, while targets in clear air were located with Z_{v}. To ensure that the targets in weather clutter were indeed targets, range Doppler maps were generated of each scan using the determined azimuth beam. In order to generate the maps, the IQ data were put through a matched filter and then through a DFT. From the range

Doppler maps, it became easier to locate targets which were inside the weather clutter and identify any which were harder to find just by looking at the PPI plots. For targets located in weather clutter, the coordinates were verified by using PSD plots. The v_{r} of the weather clutter and target at the given range could be identified using the range Doppler map, and verified by observing the peaks in the PSD.

5.1.1 Types of Targets - Single-Target Scenarios

In the single target scenarios, there are a few different target types to identify. The first is a strong target located in weather clutter. The signal is considered strong if the target signal power is more than that of the weather. Figures 5.1(a) to 5.1(f) show the PPI plots for Z_{v}, σ_{v}, and v_{r} of a strong target in weather clutter. Figures 5.1(a), 5.1(c), and 5.1(e) show the full PPI of each variable, while Figures 5.1(b), 5.1(d), and 5.1(f) show only a portion of the PPI plot with the strong target visible. The target is clearly visible in each variable. Figure 5.2(a) shows the range Doppler map of the beam at azimuth $9.14°$ with the target visible in the red box. Figure 5.2(b) shows the PSD of a strong target in weather clutter with the target in the red box and the weather in the black box.

The next type of target is a weak target in weather clutter. This case occurs when the signal power of the point target is less than that of the weather clutter. Figures 5.3(a) to 5.3(f) show the PPI plots for Z_{v}, σ_{v}, and v_{r} of a weak target in weather clutter. Figures 5.3(a), 5.3(c), and 5.3(e) show the full PPI of each variable, while Figures 5.3(b), 5.3(d), and 5.3(f) show only a portion of the PPI plot with the weak target visible. It is hard to locate the target using Z_{v} in Figure 5.3(b), but clear with σ_{v} and v_{r} in Figures 5.3(d) and 5.3(f). The σ_{v} becomes much wider with the addition of the target at a similar strength to the weather, making it easier to locate with this variable. Additionally, with the target being a different v_{r} as expected, the target looks distinct in Figure 5.3(f). Figure 5.4(a) shows the

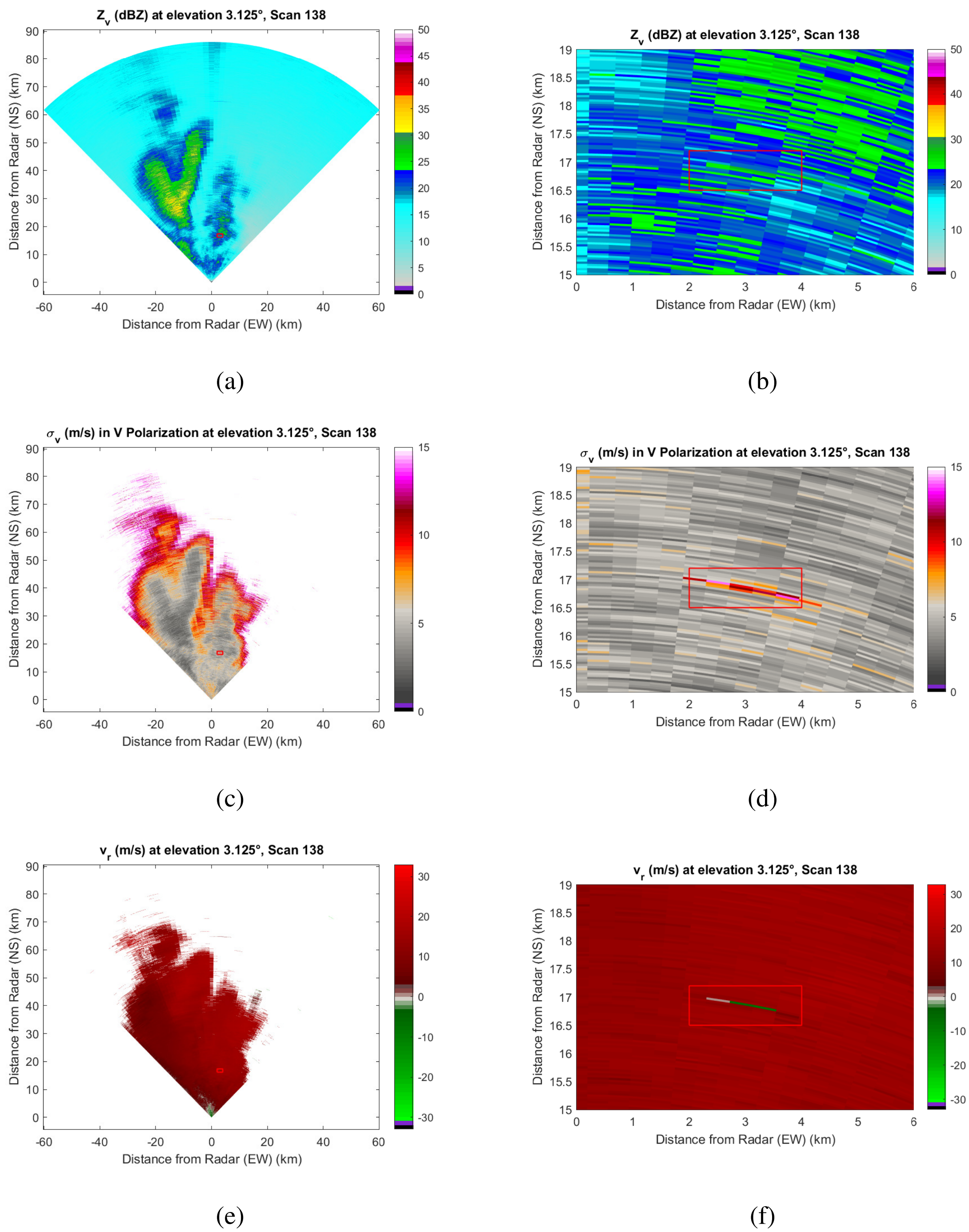

Figure 5.1: Various PPI plots for a strong target located in weather clutter. Figure 5.1(a) shows the overall PPI for Z_{v}, Figure 5.1(b) shows the PPI only around the target for Z_{v}, Figure 5.1(c) shows the PPI of σ_{v}, Figure 5.1(d) shows the PPI only around the target for σ_{v}, Figure 5.1(e) shows the PPI of v_{r}, and Figure 5.1(f) shows the PPI only around the target for v_{r}. The target's location is highlighted by a red box in each figure. This scan was taken at 22:29:42 UTC.

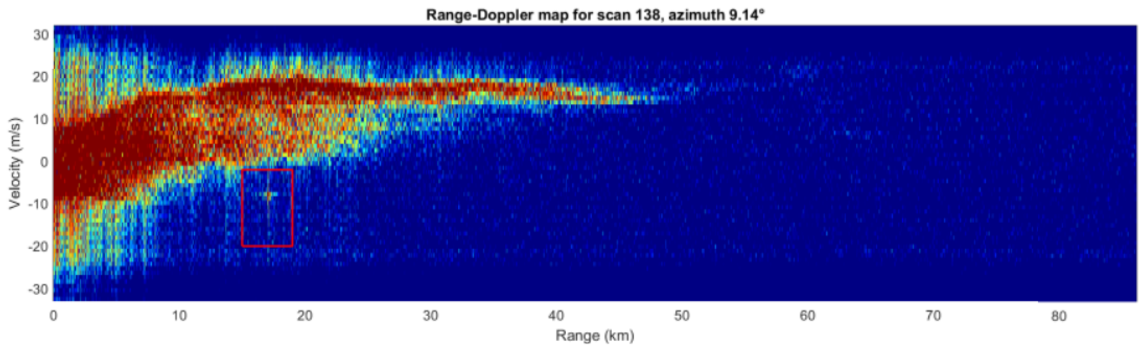

(a)

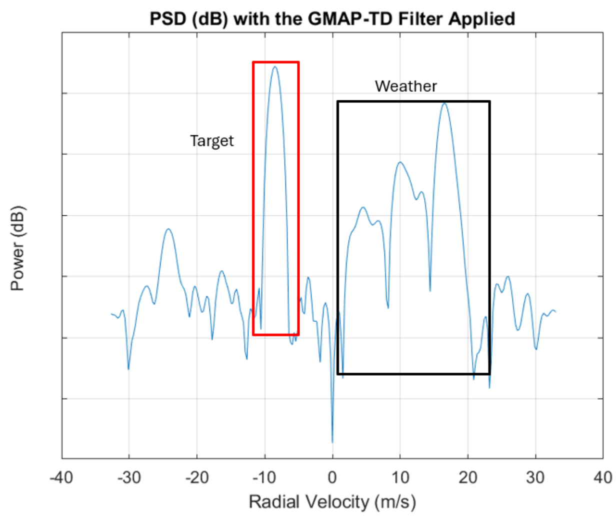

(b)

Figure 5.2: The range Doppler map and PSD for a strong target located in weather clutter. Figure 5.2(a) shows the range Doppler map for azimuth $= 9.14°$ with the target highlighted in a red box. Figure 5.2(b) shows the PSD for the target, with the target located in the red box and the weather clutter located in the black box. The strength of the target is seen to be higher than that of the weather clutter. This scan was taken at 22:29:42 UTC.

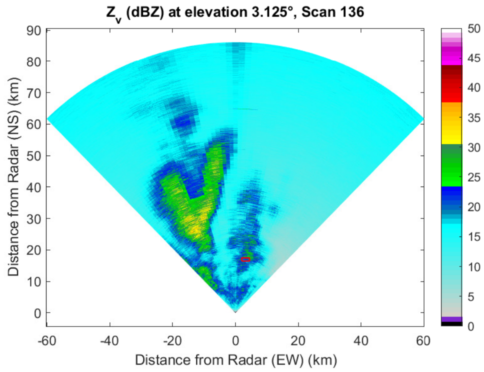

(a)

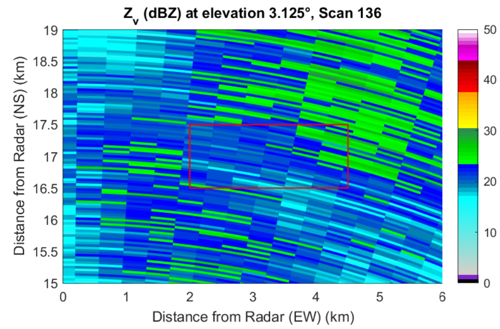

(b)

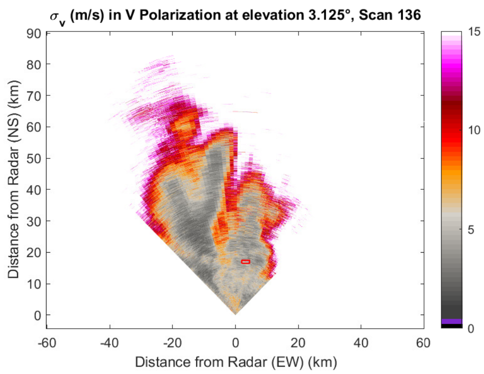

(c)

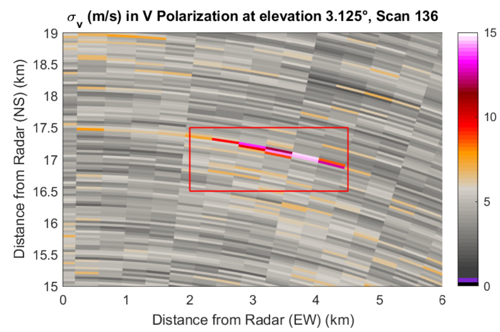

(d)

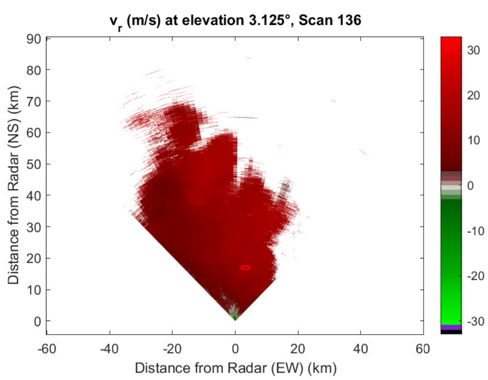

(e)

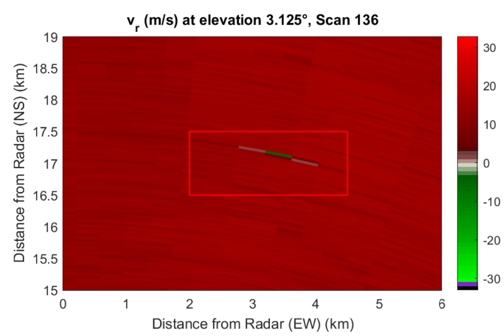

(f)

Figure 5.3: Various PPI plots for a weak target located in weather clutter. Figure 5.3(a) shows the overall PPI for Z_v, Figure 5.3(b) shows the PPI only around the target for Z_v, Figure 5.3(c) shows the PPI of σ_v, Figure 5.3(d) shows the PPI only around the target for σ_v, Figure 5.3(e) shows the PPI of v_r, and Figure 5.3(f) shows the PPI only around the target for v_r. The target's location is highlighted by a red box in each figure. This scan was taken at 22:29:36 UTC.

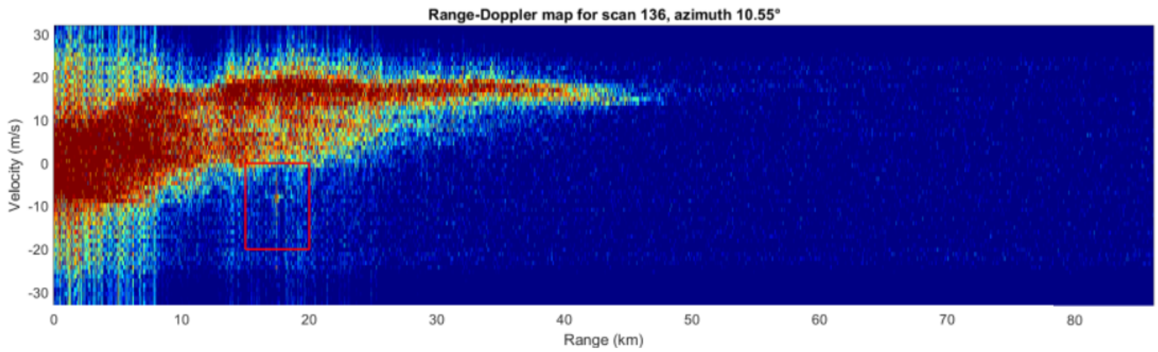

(a)

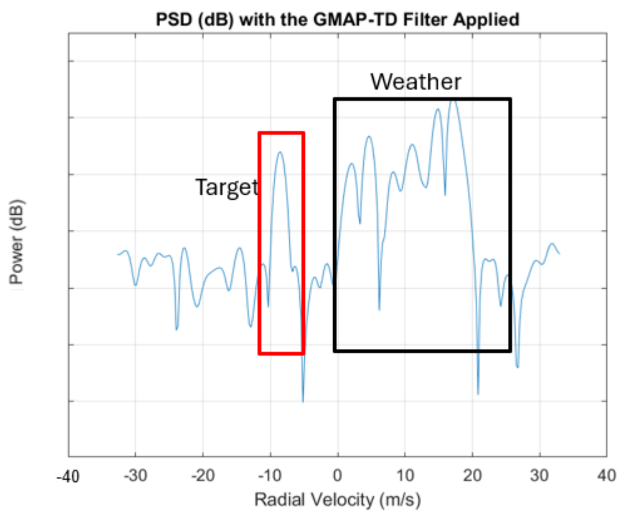

(b)

Figure 5.4: The range Doppler map and PSD for a weak target located in weather clutter. Figure 5.4(a) shows the range Doppler map for azimuth $= 10.55°$. Figure 5.4(b) shows the PSD for the target, with the target located in the red box and the weather clutter located in the black box. The strength of the target is seen to be lower than that of the weather clutter. This scan was taken at 22:29:36 UTC.

range Doppler map of the beam at azimuth $10.55°$ with the target visible in the red box. Figure 5.4(b) shows the PSD of a weak target in weather clutter with the target in the red box and the weather in the black box.

The last single target scenario in weather clutter is the case in which the v_{r} of the point target is similar to that of the weather clutter. This target type is more difficult to identify, as it will appear within the weather clutter in the range Doppler map rather than as a separate, clear target. In order to identify this type of target, targets were tracked throughout multiple range Doppler maps to estimate the position. Various PSDs will be shown for this case in Section 5.2.4.

The final single target scenario is a target located in clear air. There is no strong or weak case for this target, as there is no weather clutter present with which to compare the strength. Figures 5.5(a) to 5.5(f) show the PPI plots for Z_{v}, σ_{v}, and v_{r} of a target in clear air. Figures 5.5(a), 5.5(c), and 5.5(e) show the full PPI of each variable, while Figures 5.5(b), 5.5(d), and 5.5(f) show only a portion of the PPI plot with the target visible. The v_{r} in Figures 5.5(e) and 5.5(f) is censored where the SNR $< 2\,dB$, so the target is still visible. Figure 5.6(a) shows the range Doppler map of the beam at azimuth $2.11°$ with the target visible in the red box. Figure 5.6(b) shows the PSD of a weak target in weather clutter with the target in the red box. No weather clutter is present, which is clear in the PSD.

5.1.2 Types of Targets - Multiple-Target Scenarios

In a multiple target scenario, the same types of targets are identified as with the single target scenario. With this case, there may be strong and weak targets located together in the weather clutter or in clear air. For the multiple target scenarios, there is one real point target followed by up to 16 “simulated” targets generated as described in Section 4.1.1. The simulated targets are spaced about $1.5\,km$ in range within the same azimuth beam. Recall

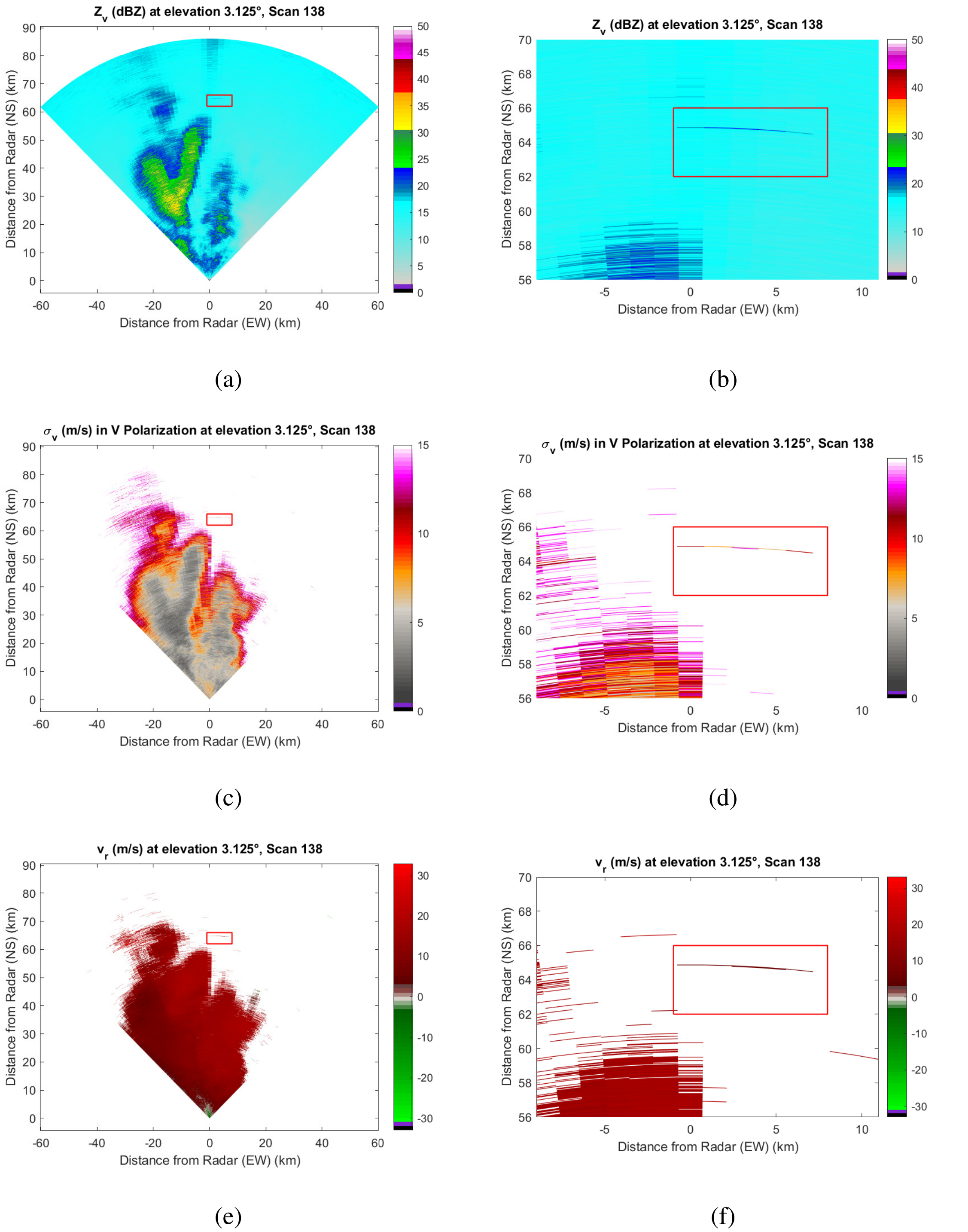

Figure 5.5: Various PPI plots for a target located in clear air. Figure 5.5(a) shows the overall PPI for Z_v, Figure 5.5(b) shows the PPI only around the target for Z_v, Figure 5.5(c) shows the PPI of σ_v, Figure 5.5(d) shows the PPI only around the target for σ_v, Figure 5.5(e) shows the PPI of v_r, and Figure 5.5(f) shows the PPI only around the target for v_r. The target's location is highlighted by a red box in each figure. This scan was taken at 22:29:42 UTC.

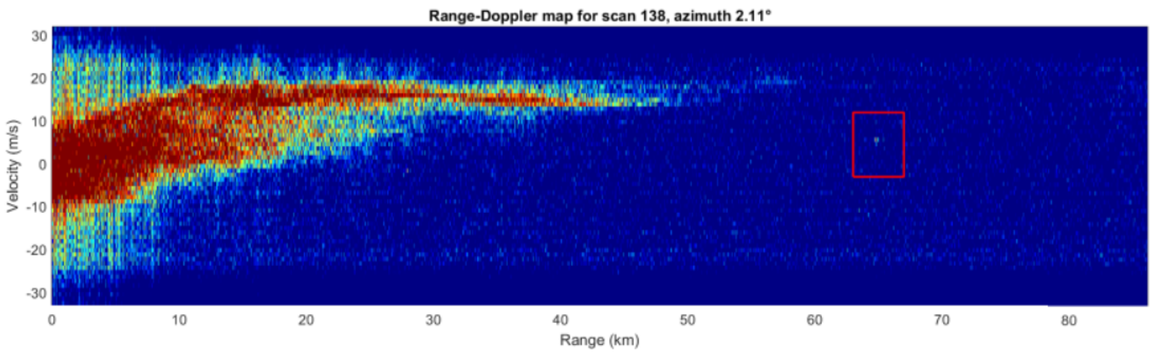

(a)

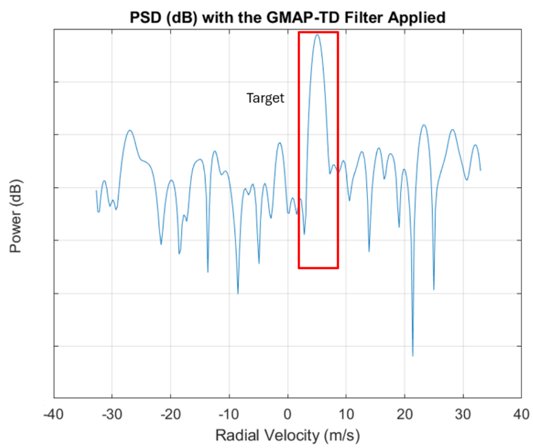

(b)

Figure 5.6: The range Doppler map and PSD for a target located in clear air. Figure 5.6(a) shows the range Doppler map for azimuth $= 2.11°$. Figure 5.6(b) shows the PSD for the target, with the target located in the red box. This scan was taken at 22:29:42 UTC.

from Table 4.2 that the guard band is $40\,m$ on either side of the CUT and the training band is $360\,m$ on either side of the CUT. This totals to $400\,m$, which is less than the $1.5\,km$ spacing of the targets, so there will be no target interference in the training bands with this data.

The first scenario for the multiple targets case is for targets in weather clutter. Figures 5.7(a) to 5.7(f) show the PPI plots for Z_{v}, σ_{v}, and v_{r} with multiple targets in weather clutter. Figures 5.7(a), 5.7(c), and 5.7(e) show the full PPI of each variable, while Figures 5.7(b), 5.7(d), and 5.7(f) show only a portion of the PPI plot with the targets visible. The azimuth beam along which the targets are aligned is outlined in red in Figures 5.7(b), 5.7(d), and 5.7(f). Figure 5.8(a) shows the range Doppler map of the beam at azimuth $-2.11°$ with the targets visible in the red box. Figure 5.8(b) shows the PSD of a strong target in weather clutter, while Figure 5.8(c) shows the PSD of a weak target in weather clutter. In both figures, the target is located in the red box and the weather in the black box. Of the seventeen targets located in this volume, twelve were identified as strong targets and the remaining five were considered weak in comparison to the weather clutter. Additionally, some of the targets are located along the edge of the weather clutter, which can be seen clearly in Figures 5.7(d) and 5.7(f).

There is also the scenario in which multiple targets are located in clear air. Figures 5.9(a) to 5.9(f) show the PPI plots for Z_{v}, σ_{v}, and v_{r} of multiple targets in clear air. Figures 5.9(a), 5.9(c), and 5.9(e) show the full PPI of each variable, while Figures 5.9(b), 5.9(d), and 5.9(f) show only a portion of the PPI plot with the targets visible. As with the multiple target case in weather clutter, the azimuth beam along which the targets are aligned is outlined in red in Figures 5.9(b), 5.9(d), and 5.9(f). Figure 5.10(a) shows the range Doppler map of the beam at azimuth $-2.11°$ with the targets visible in the red box. Figure 5.10(b) shows the PSD of one of the targets, with the target is located in the red box. As mentioned for the single target clear air case, the targets are not considered strong or weak in this

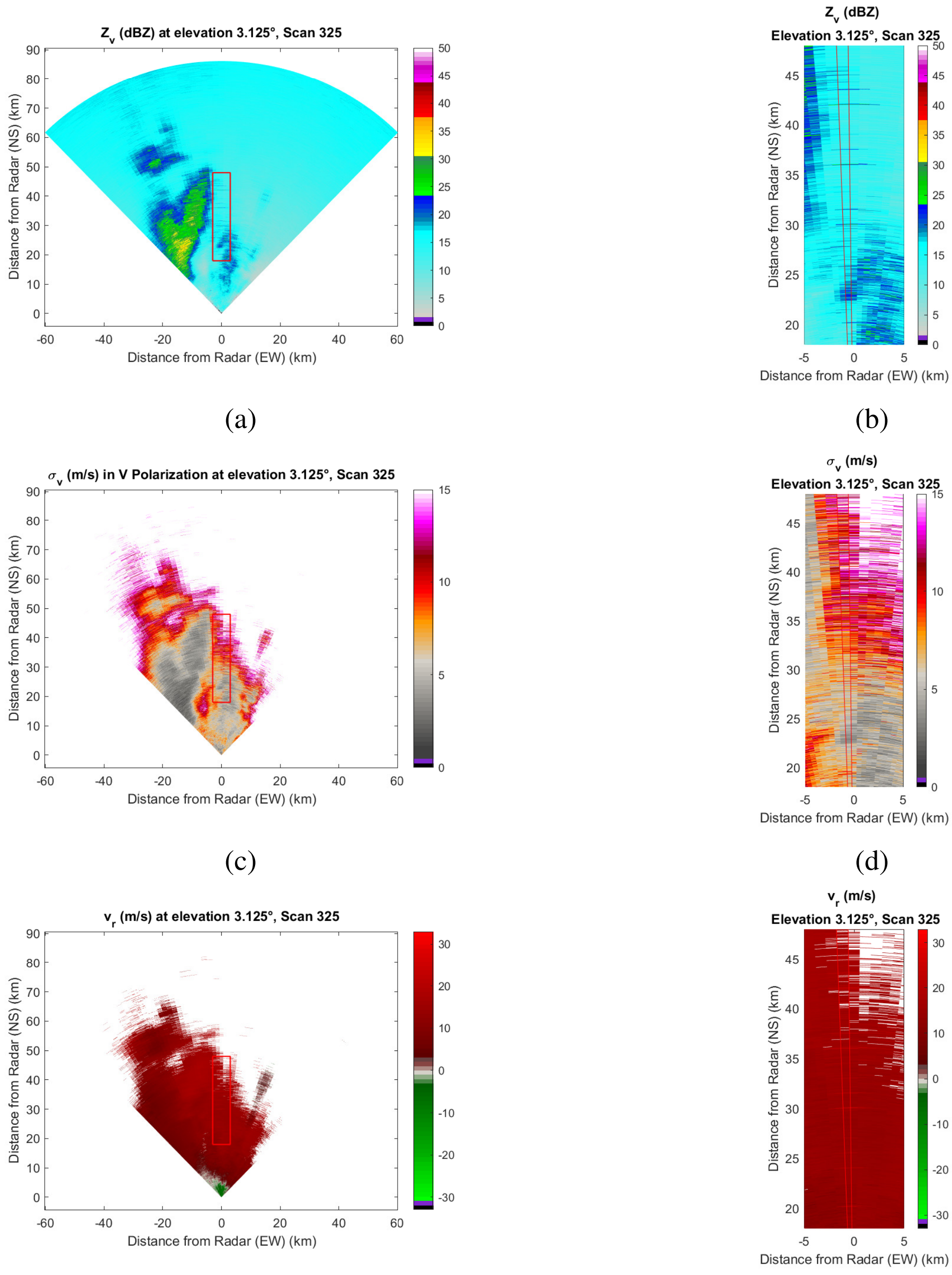

(a) (b) (c) (d) (e) (f)

Figure 5.7: Various PPI plots for multiple targets located in weather clutter. Figure 5.7(a) shows the overall PPI for Z_{v}, Figure 5.7(b) shows the PPI only around the target for Z_{v}, Figure 5.7(c) shows the PPI of σ_{v}, Figure 5.7(d) shows the PPI only around the target for σ_{v}, Figure 5.7(e) shows the PPI of v_{r}, and Figure 5.7(f) shows the PPI only around the target for v_{r}. The target's location is highlighted by a red box in each figure. The azimuthal beam ($-2.11°$) which the targets are located in is highlighted in Figures 5.7(b), 5.7(d), and 5.7(f). This scan was taken at 22:39:10 UTC.

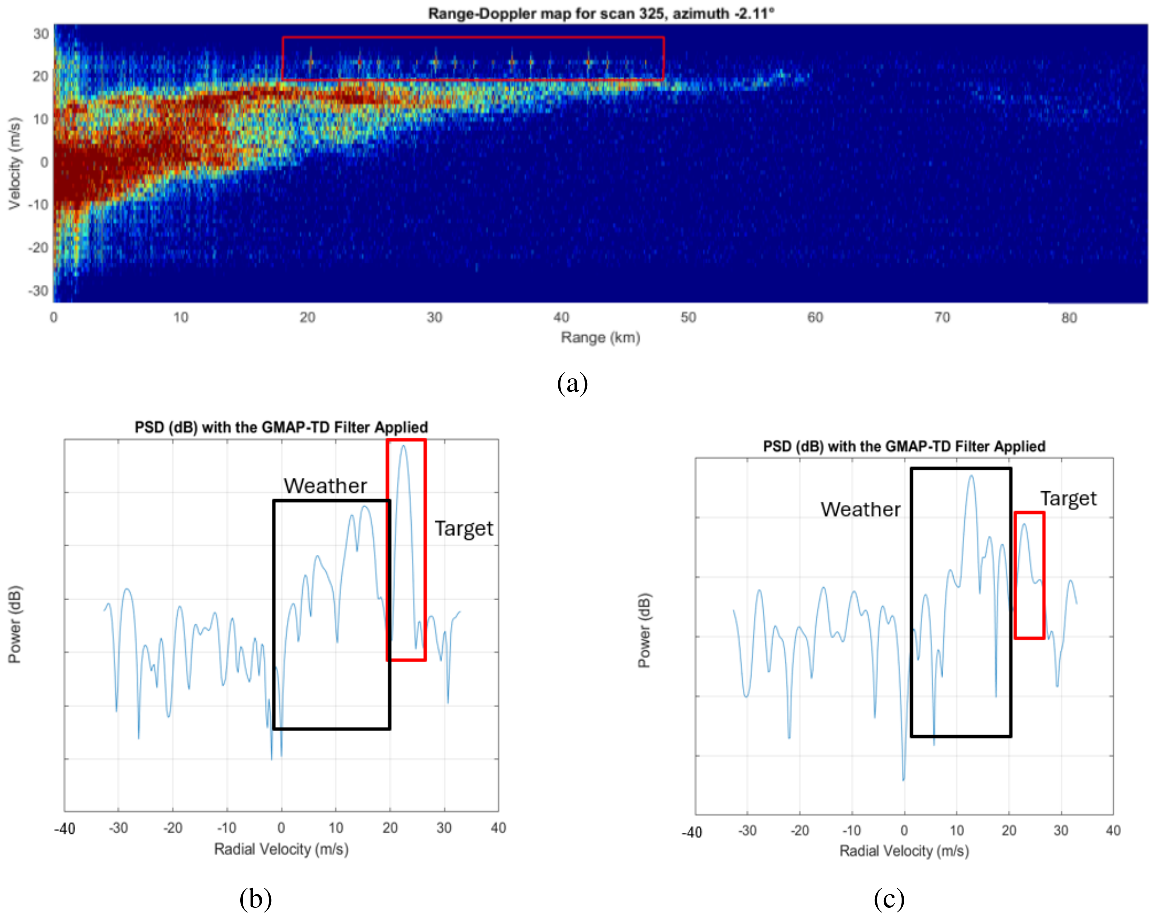

Figure 5.8: The range Doppler map and PSD plots for a strong and weak target in the multiple target case located in weather clutter. Figure 5.8(a) shows the range Doppler map for azimuth $= -2.11°$. Figure 5.8(b) shows a strong target compared to the weather clutter, while Figure 5.8(c) shows a weak target compared to the weather clutter, with the target located in the red box and the weather located in the black box in both figures. This scan was taken at 22:39:10 UTC.

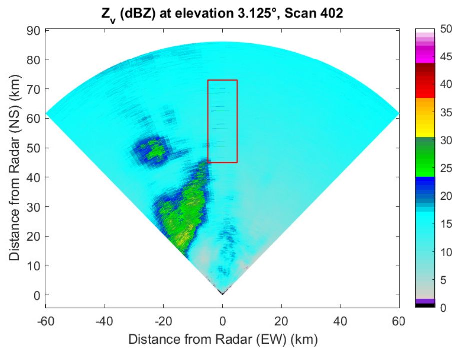

(a)

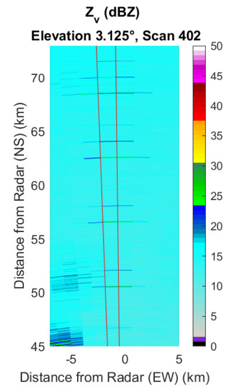

(b)

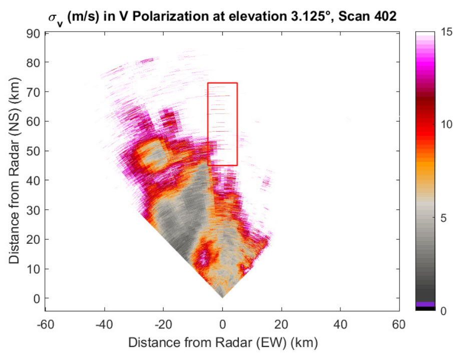

(c)

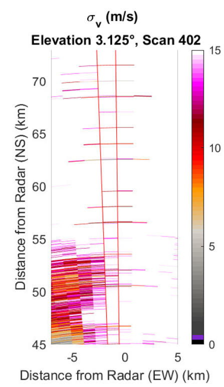

(d)

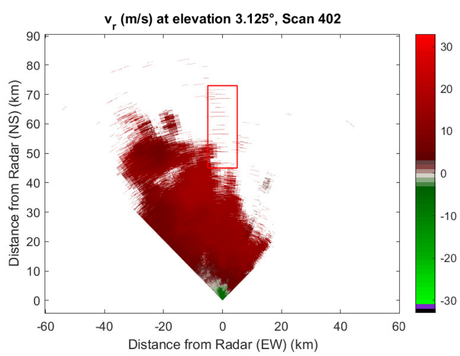

(e)

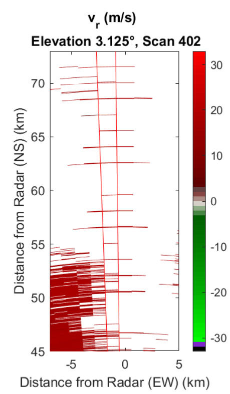

(f)

Figure 5.9: Various PPI plots for multiple targets located in clear air. Figure 5.9(a) shows the overall PPI for Z_v, Figure 5.9(b) shows the PPI only around the target for Z_v, Figure 5.9(c) shows the PPI of σ_v, Figure 5.9(d) shows the PPI only around the target for σ_v, Figure 5.9(e) shows the PPI of v_r, and Figure 5.9(f) shows the PPI only around the target for v_r. The target locations are highlighted by a red box in each figure. The azimuthal beam ($-2.11°$) which the targets are located in is highlighted in Figures 5.7(b), 5.7(d), and 5.7(f). This scan was taken at 22:43:03 UTC.

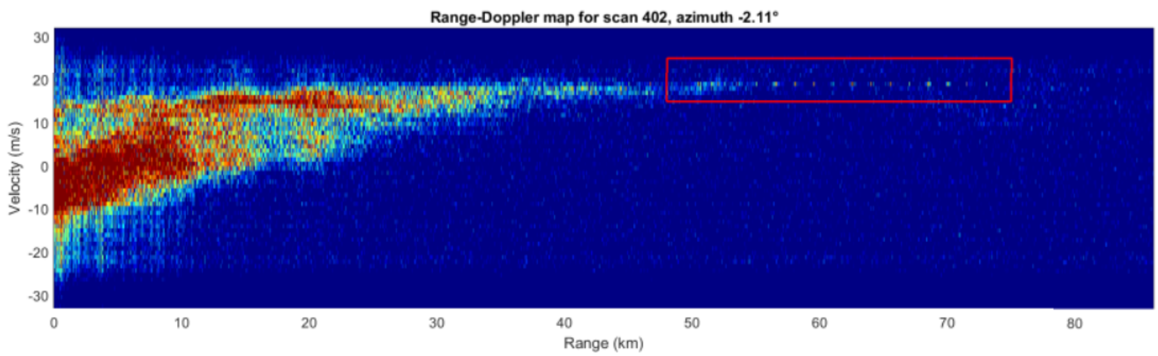

(a)

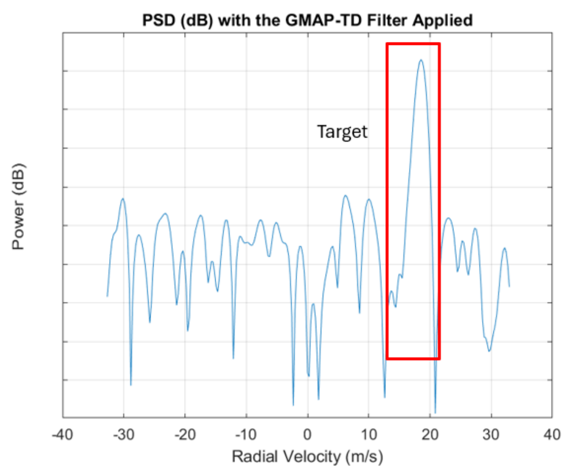

(b)

Figure 5.10: The range Doppler map and PSD plots for the multiple target case located in clear air. Figure 5.10(a) shows the range Doppler map for azimuth $= -2.11°$. Figure 5.10(b) shows a the PSD of one of the targets, with the target located in the red box and the weather located in the black box in both figures. This scan was taken at 22:43:03 UTC.

Table 5.1: False Alarm Rates of the Various Algorithms

Algorithm	False Alarm Rate ($P_{FA} = 10^{-1}$)	False Alarm Rate ($P_{FA} = 10^{-2}$)
Z_{v} OS-CFAR	2.5×10^{-3}	3.93×10^{-5}
σ_{v} IQR-CFAR	5.3×10^{-3}	2.39×10^{-5}
v_{r} IQR-CFAR	3.0×10^{-3}	1.17×10^{-4}

scenario, as there is no clutter with which to compare the strength of the targets. The v_{r} in Figures 5.9(e) and 5.9(f) is censored where the SNR $< 2\,dB$, so the target is still visible. A total of fifteen targets were identified in the volume scan shown.

5.2 Comparative Results from the CFAR Algorithms

With targets identified, the first step in observing the effectiveness of the algorithm is determining the false alarm rate of the algorithm with clutter present. Each individual variable CFAR algorithm is analyzed, along with the Wx-CFAR algorithm. Table 5.1 shows the false alarm rate of the various single variable algorithms during volume scans which no aircraft are present, and Table 5.2 shows the results for the various confidence levels of the Wx-CFAR algorithm in the same volume scans. The false alarm rate is calculated with

$$False\,Alarm\,Rate = \frac{Number\,of\,false\,alarms}{Total\,number\,of\,cells} \tag{5.1}$$

When determining which variables should hold more weight in the Wx-CFAR algorithm, considering the actual false alarm rate was paramount. The goal of the algorithm is to reduce false alarms while maintaining a higher number of detections, so it is important to observe which variables perform best in clutter. Based on Table 5.1, it is clear that σ_{v} has a much higher false alarm rate than Z_{v} or v_{r} when the ideal P_{FA} is set to 10^{-1}. This is prevalent primarily in clear air, where the σ_{v} is much higher than it is for weather clutter or

Table 5.2: False Alarm Rates of the Wx-CFAR Algorithm

Confidence	False Alarm Rate ($P_{FA} = 10^{-1}$)	False Alarm Rate ($P_{FA} = 10^{-2}$)
≥ 1.5	2.4×10^{-3}	8.94×10^{-5}
≥ 2.5	2.26×10^{-4}	2.59×10^{-5}
≥ 2.75	1.22×10^{-4}	6.55×10^{-7}
≥ 3.75	3.11×10^{-5}	6.55×10^{-7}

point targets, but is also noisier than Z_{v}, which maintains a similar level throughout clear air. The variability in σ_{v} does not cause as many false alarms when decreasing the desired P_{FA} to 10^{-2}.

Figures 5.11(a), 5.11(c), and 5.11(e) show the PPI maps of Z_{v}, σ_{v}, and v_{r}, respectively, while Figures 5.11(b), 5.11(d), and 5.11(f) show detection map PPIs for the Z_{v}, σ_{v}, and v_{r} single variable algorithms with only weather clutter present using an ideal P_{FA} of 10^{-1}. Looking at the individual variable detection maps when comparing to the shape of the weather in the PPI maps of the variables shows the strengths and weaknesses of each variable.

Figure 5.11(b) shows that there are few false alarms in clear air while using Z_{v}, but several throughout the weather clutter. Figure 5.11(f) shows that detecting with v_{r} gives a concentration of false alarms along the clutter edge, where the weather clutter hits clear air. This variable is then primarily useful when the target and the surrounding training band are fully located in the weather clutter, with limitations along the clutter edge. Additionally, it is not useful in clear air, as discussed in Section 4.4. Figure 5.11(d) shows a relatively high number of false alarms in both clear air and weather clutter for detection with σ_{v}. Locating a point target with σ_{v} on its own then becomes challenging due to the high false alarms present. Although this is not an ideal variable for detection on its own, it is still useful to gain further information on the target, which will be seen once the detection results of

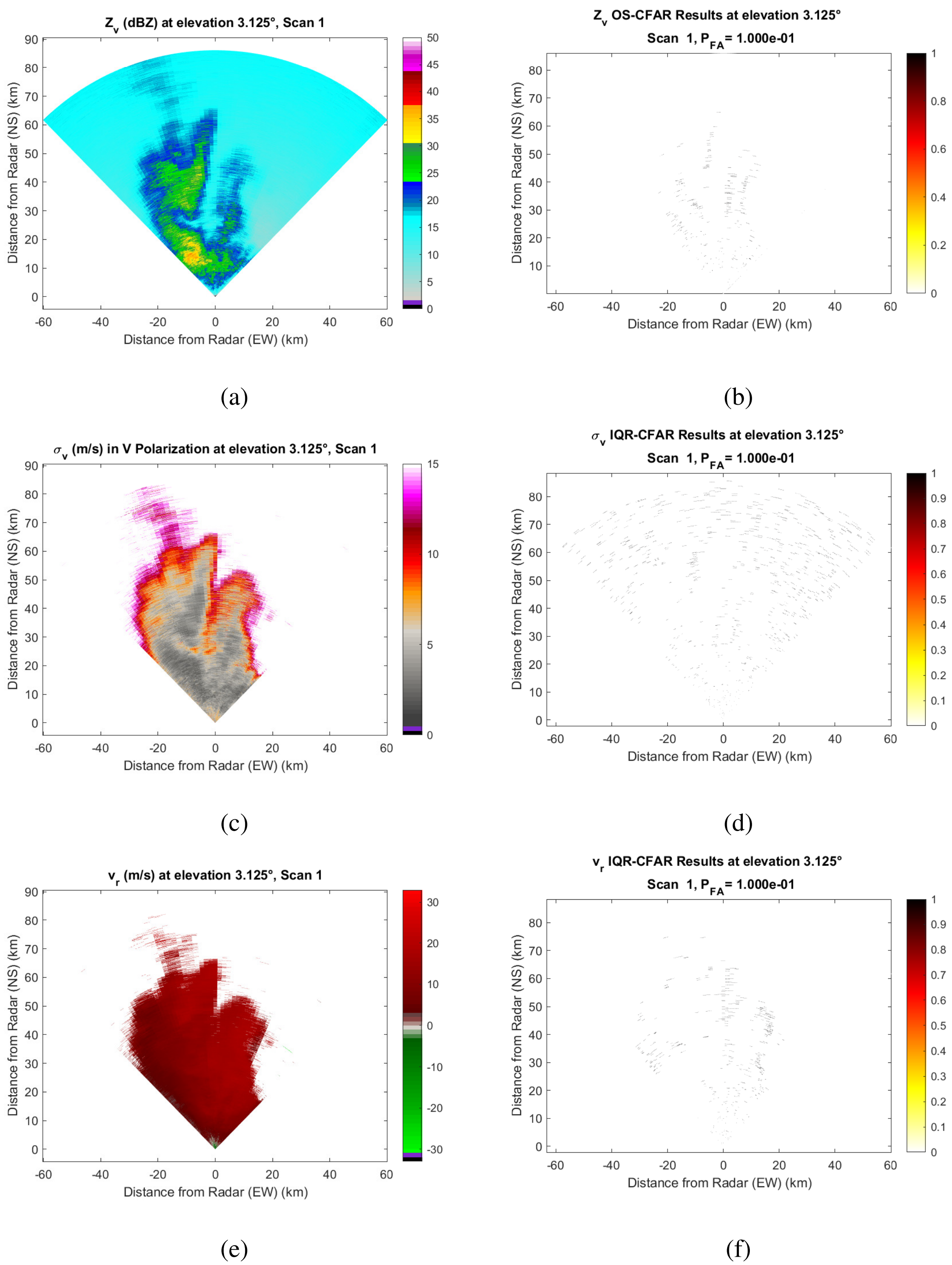

Figure 5.11: Detection PPI plots for the various CFAR algorithms with only weather clutter present and the respective weather variable PPI plots as comparison. Figures 5.11(a), 5.11(c), and 5.11(e) are the PPI plots for Z_v, σ_v, and v_r, respectively. Figures 5.11(b), 5.11(d), and 5.11(f) are the detection PPI using Z_v, σ_v, and v_r, respectively. All CFAR PPI plots use a P_{FA} of 10^{-1}. This scan was taken at 22:22:46 UTC.

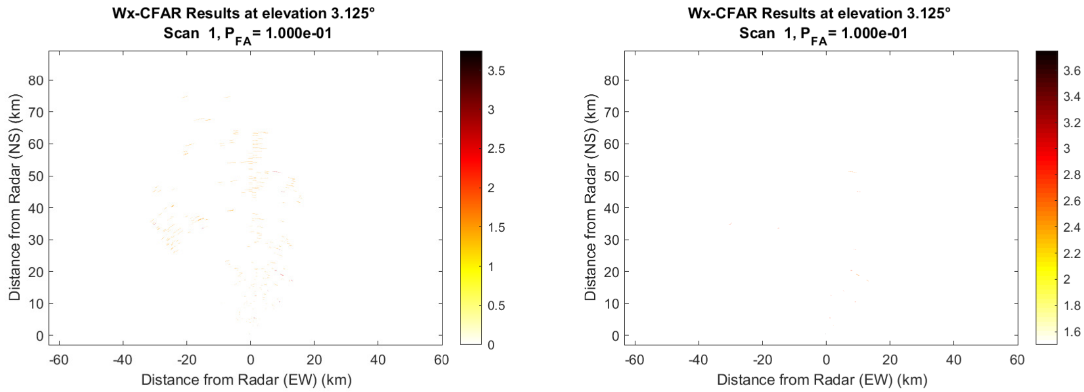

(a) (b)

Figure 5.12: Detection PPI plot for the Wx-CFAR algorithm with only weather clutter present. The Wx-CFAR algorithm uses a P_{FA} of 10^{-1}. Figure 5.12(a) shows detections of all levels of confidence, while Figure 5.12(b) shows only detections above a confidence of 1.5. This scan was taken at 22:22:46 UTC.

specific targets are presented.

Finally, Figures 5.12(a) and 5.12(b) show the improvements gained with the Wx-CFAR algorithm in regards to false alarms. Figure 5.12(a) shows that the algorithm still has many detections, but none stand out as a higher confidence. Looking at Figure 5.12(b) confirms this, with the weakest false alarms being censored. Limited detections still remain, and few appear to be at the highest confidence. Table 5.2 corroborates these results, showing that the false alarm rate is significantly reduced when switching which variable is used in clear air or weather clutter. When looking at all detections regardless of confidence level, the false alarm rate is lower than any rate shown in Table 5.1 due to the optimization for each scenario. Additionally, there are significantly fewer false alarms as confidence is gained.

5.2.1 Single-Target Scenarios

Now that various target scenarios have been identified and false alarm rates discussed, the results of the individual variable algorithms and the Wx-CFAR algorithm in regards

Table 5.3: Results of Detection of Various Single Target Scenarios

Signal Strength	Clutter Presence	P_{FA}	Z_{v}	σ_{v}	υ_{r}
Weak	Weather Clutter	10^{-1}	N	D	D
Strong	Weather Clutter	10^{-1}	P	D	D
-	Clear Air	10^{-1}	D	D	N
Weak	Weather Clutter	10^{-2}	N	D	D
Strong	Weather Clutter	10^{-2}	N	P	D
-	Clear Air	10^{-2}	D	N	N

to detection can be analyzed. Table 5.3 shows detections for the individual algorithms on various targets with two different ideal P_{FA} selections. Although the chosen P_{FA} are higher than what is typical for a detection algorithm, many detections are lost just from $P_{FA} = 10^{-1}$ to $P_{FA} = 10^{-2}$, and it becomes nearly impossible to detect targets in clutter at better P_{FA} selections. When considering the false alarm rates shown in Tables 5.1 and 5.2, this result makes intuitive sense. Most importantly, the number of false alarms decreases by up to three orders of magnitude, so it follows that the number of detections will also decrease.

The last three columns in Table 5.3 indicate whether the target was detected with *D* for detection, *N* for no detection, and *P* for a partial detection. An example of a partial detection can be seen in Figures 5.13(a) and 5.13(b). These figures show that the central portion of the target is missing in the σ_{v} detection using a P_{FA} of 10^{-2}. The results of detection verify that υ_{r} is not useful in clear air, but beneficial when there is clutter present. Inversely, Z_{v} is useful in clear air but in the presence of clutter, it weakens. It manages a partial detection when the ideal P_{FA} is set to 10^{-1} for the strong target in weather clutter, but does not locate the weaker target. Additionally, σ_{v} detects all targets when $P_{FA} = 10^{-1}$. Despite the good performance of σ_{v} for detection in both clear air and weather clutter, it was not considered as the first variable in either scenario due to the high false alarm rate as

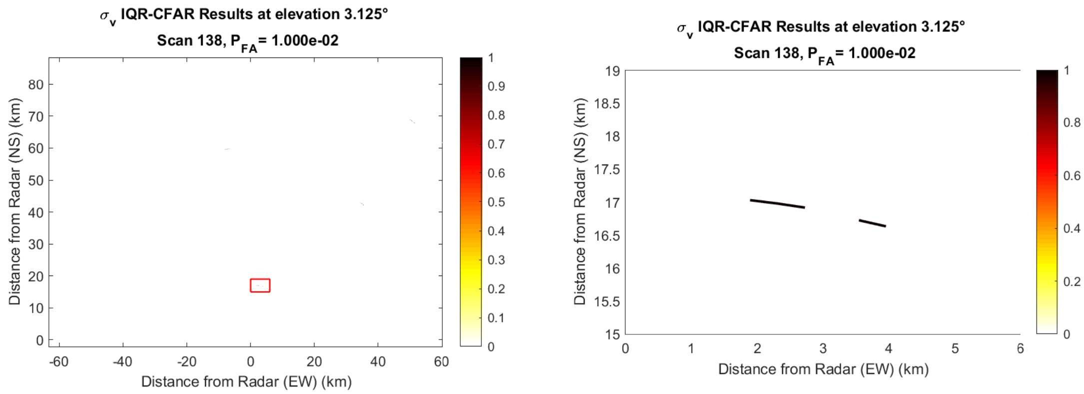

(a) (b)

Figure 5.13: The partial detection of a target in σ_{v}. The target is located in weather clutter with a similar signal power to the surrounding clutter. The ideal P_{FA} is set to 10^{-2}. Figure 5.13(a) shows the overall detection PPI for σ_{v} with the target outlined in a red box, while Figure 5.13(b) shows only the contents in the red box.

seen in Table 5.1.

5.2.2 Multiple-Target Scenarios

The multiple targets cases provide distinct results for the case of this algorithm. Table 5.4 shows the results of the multiple targets identified in clear air and weather clutter. For the weather clutter, there were five weak targets and twelve strong targets identified for a total of seventeen targets. In clear air, a total of fifteen targets were identified. σ_{v} has trouble with the data located in weather clutter because the v_{r} of the target is near that of the clutter. The spectrum does not change much due to this, so the target is not identified. Different data for a multiple-target case may provide more favorable results for σ_{v} in weather clutter, as seen in the single target cases. This will be analyzed more in Section 5.2.4. In clear air, σ_{v} performs much better when $P_{FA} = 10^{-1}$ but does not detect any targets when $P_{FA} = 10^{-2}$. For weak targets in weather clutter, v_{r} misses one target while the remaining variables do not detect any. For strong targets in clutter, v_{r} locates all of them while Z_{v} only detects half.

Table 5.4: Results of Detection of Various Multiple Target Scenarios

Signal Strength	Clutter Presence	P_{FA}	Z_v	σ_v	v_r
Weak	Weather Clutter	10^{-1}	0%	0%	80%
Strong	Weather Clutter	10^{-1}	50%	0%	100%
-	Clear Air	10^{-1}	60%	66.67%	0%
Weak	Weather Clutter	10^{-2}	0%	0%	0%
Strong	Weather Clutter	10^{-2}	16.7%	0%	50%
-	Clear Air	10^{-2}	46.67%	0%	0%

The clear-air results for Z_v and σ_v are interesting because there are multiple targets which are detected by one variable and not the other. Additionally, σ_v has one more detection than Z_v with $P_{FA} = 10^{-1}$. Ultimately, Z_v is still used first in clear air to avoid the false alarms from σ_v, despite having one less detection.

5.2.3 Benefits of the Wx-CFAR Algorithm

Multiple benefits of the Wx-CFAR algorithm were identified during analysis. The benefits include improved detection in weather clutter and reduction of false alarms through both confidence level and switching which variable is chosen. Additionally, the selection and benefit of using weights is explained.

Figures 5.14(a), 5.14(c), and 5.14(e) show the detection PPI plots for Z_v, σ_v, and v_r for multiple targets in weather clutter with the location of the targets outlined with a red box, and Figures 5.14(b), 5.14(d), and 5.14(f) show only the area highlighted by the red box, with the location of the targets highlighted by colored dots along one azimuthal beam. There is significant clutter in both Figure 5.14(b) and in Figure 5.14(f) surrounding the point targets. Additionally, Figure 5.14(d) shows that σ_v does not detect any targets, which was explained in Section 5.2.2.

Figures 5.15(a) and 5.15(b) show the results of the Wx-CFAR algorithm prior to fil-

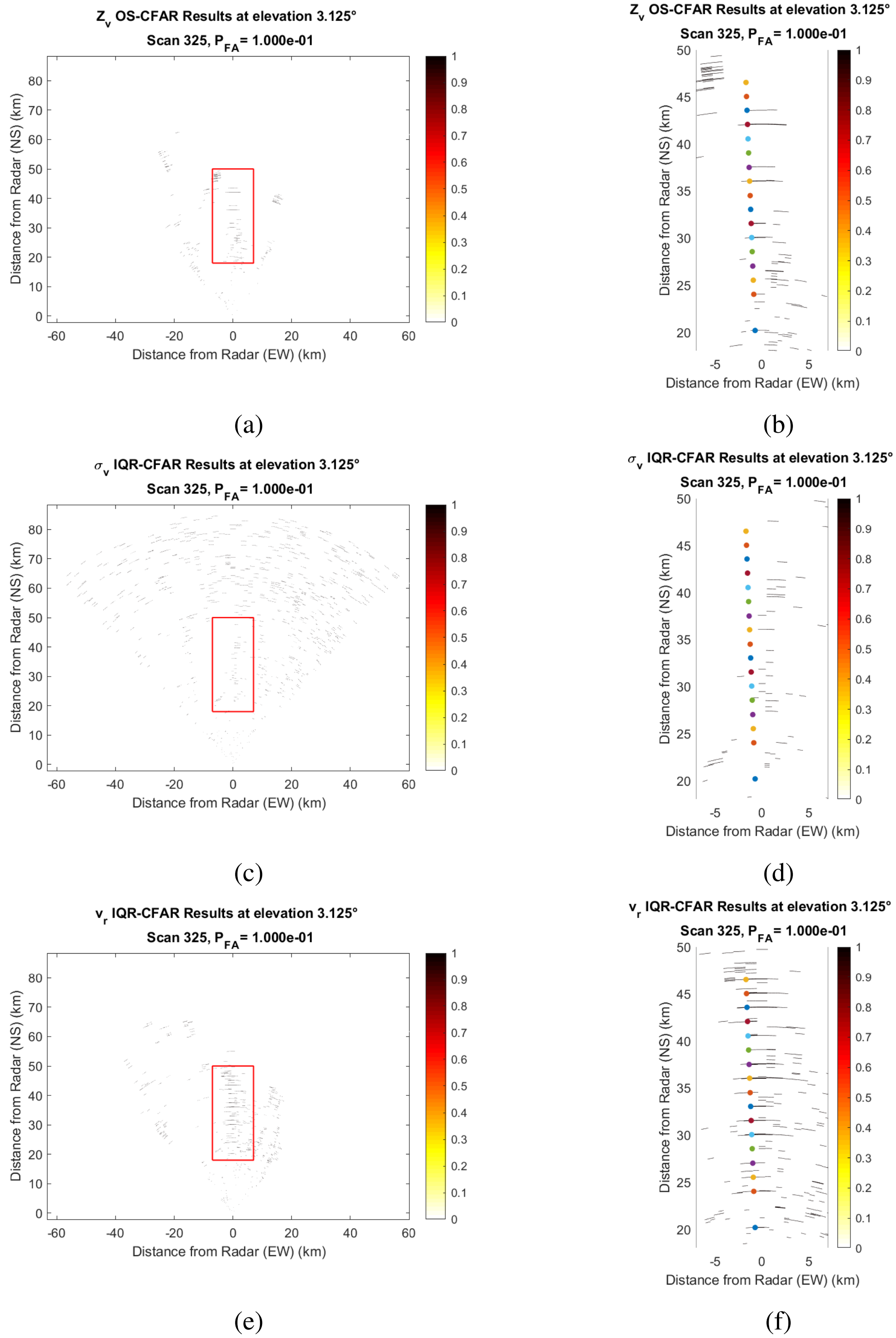

Figure 5.14: The results of the Z_{v} based OS-CFAR algorithm (Figures 5.14(a) and 5.14(b)), of the σ_{v} based IQR-CFAR algorithm (Figures 5.14(c) and 5.14(d)), and of the v_{r} based IQR-CFAR algorithm (Figures 5.14(e) and 5.14(f)) for a multiple target case in weather clutter. The colored dots in Figures 5.14(b), 5.14(d), and 5.14(f) indicate the position of a known target. This scan was taken at 22:39:10 UTC.

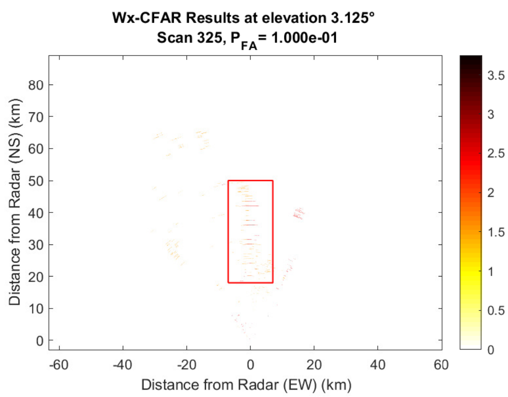

(a)

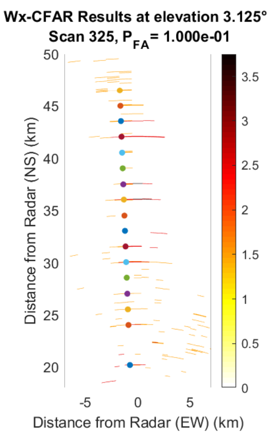

(b)

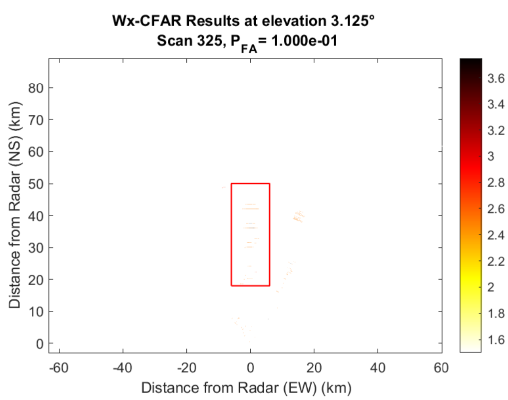

(c)

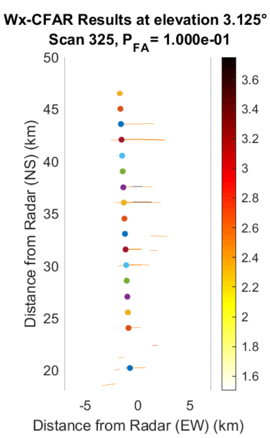

(d)

Figure 5.15: The results of the Wx-CFAR algorithm for a multiple target case in weather clutter. Figures 5.15(a) and 5.15(b) show the results without filtering out any confidence level. Figures 5.15(c) and 5.15(d) show the results where only detections above a confidence level of 1.5 are shown. The colored dots in Figures 5.15(b) and 5.15(d) indicate the position of a known target. This scan was taken at 22:39:10 UTC.

tering. There is still some clutter observed near the targets at low confidence. When only detections greater than 1.5 in confidence are shown in Figures 5.15(c) and 5.15(d), significant amounts of clutter are reduced. This results in the loss of six targets which were detected only in v_r. As mentioned in Section 5.2.2, σ_v does not widen much for this data, so these results are only improved by Z_v. With more variation in v_r and σ_v as shown in Section 5.2.1, fewer targets may be lost. This is demonstrated in Figures 5.16(a) to 5.17(d), which are the detection results for a weak target in weather clutter case.

Figures 5.16(a), 5.16(c), and 5.16(e) show the detection PPI plots for Z_v, σ_v, and v_r for a weak target in weather clutter with the location of the targets outlined with a red box, and Figures 5.16(b), 5.16(d), and 5.16(f) show only the area highlighted by the red box in the full PPI plots, with the location of the target highlighted by a red box. The point target identified by these plots is a different v_r of the weather clutter, but has a weaker signal. It is not detected in Z_v, but easily detected with v_r and σ_v. Figures 5.17(a) and 5.17(b) show the results of the Wx-CFAR algorithm with all confidence levels visible. The confidence for this target is 2.75, making it easily identifiable when the algorithm filters out results at confidence 1.5 in Figures 5.17(c) and 5.17(d). These figures also show the target in clear air identified in Section 5.1.1, located at approximately $65\,km$ from the radar in the Y-axis and $0-5\,km$ from the radar in the X-axis. This target is detected at full confidence. The results show few false alarms above a confidence level of 1.5 in Figures 5.17(c) and 5.17(d), with the two targets appearing clearly.

Improved Detection

When choosing an ideal P_{FA}, typically a maximum of 10^{-3} is desired. In the instance of a target located in weather clutter, using this P_{FA} will result in few, if any, detections. However, using a greater P_{FA} which allows for more detections results in a higher false alarm rate. It becomes hard to identify whether a detection is a false alarm or a true detection

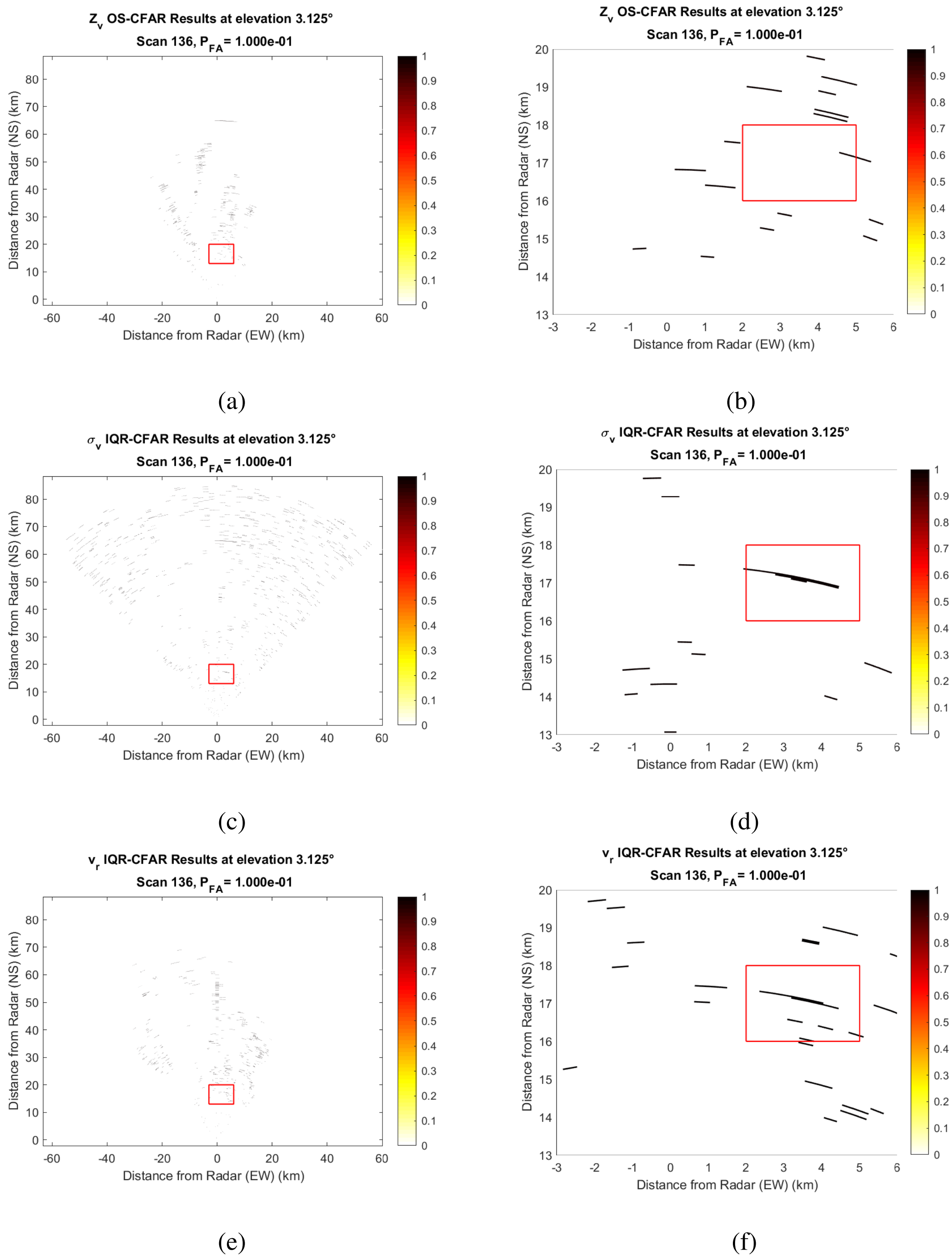

Figure 5.16: The results of the Z_{v} based OS-CFAR algorithm (Figures 5.16(a) and 5.16(b)), of the σ_{v} based IQR-CFAR algorithm (Figures 5.16(c) and 5.16(d)), and of the v_{r} based IQR-CFAR algorithm (Figures 5.16(e) and 5.16(f)) for a single target case in weather clutter. The target is located in the red box. This scan was taken at 22:29:36 UTC.

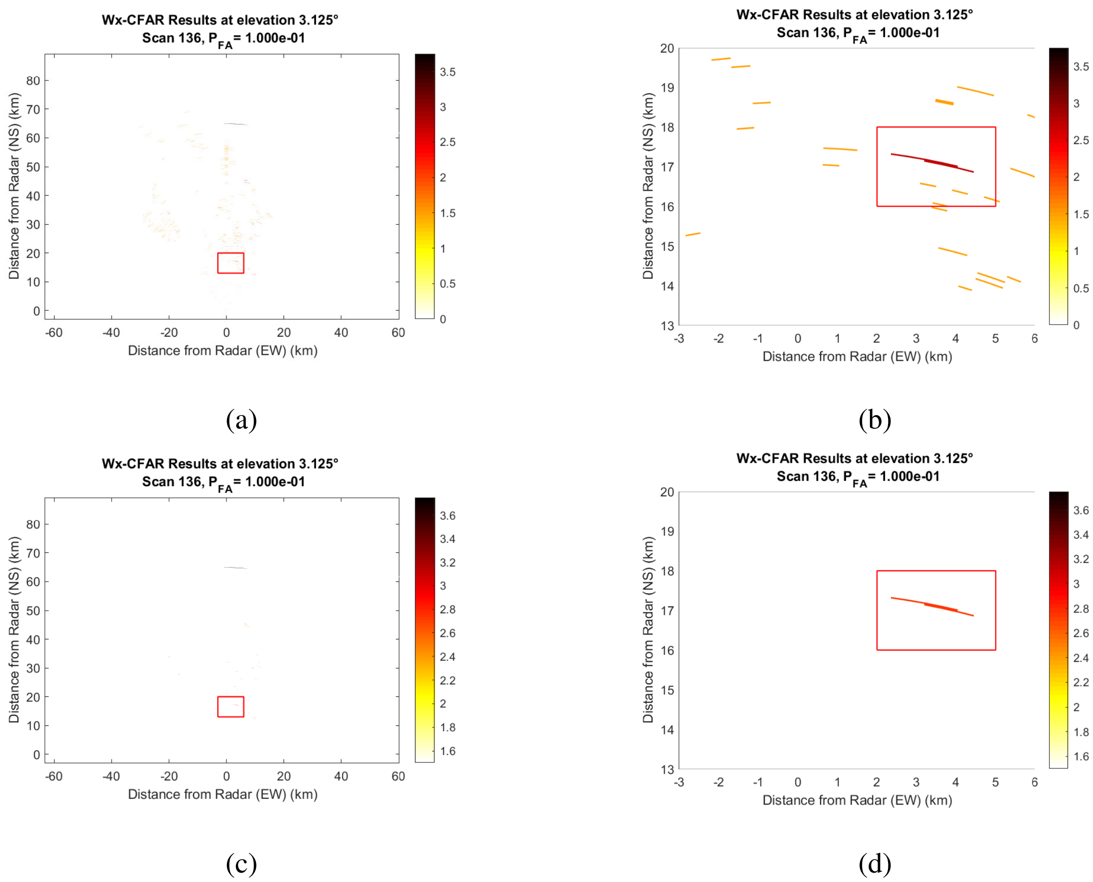

Figure 5.17: The results of the Wx-CFAR algorithm for a single target case in weather clutter. Figures 5.17(a) and 5.17(b) show the results without filtering out any confidence level. Figures 5.17(c) and 5.17(d) show the results where only detections above a confidence level of 1.5 are shown. The red box indicates the location of the known target. This scan was taken at 22:29:36 UTC.

when the false alarm rate increases in single variable CFAR algorithms. The Wx-CFAR algorithm allows the use of a greater P_{FA} while mitigating excess false alarms with the increased confidence, which was demonstrated in Table 5.2 and Figure 5.12(a).

The increase of detections is particularly noticed in weather clutter when compared to traditional power-based CFAR algorithms. Although Z_{v} can identify strong targets in weather clutter, there is some difficulty with weaker targets. The results of the Wx-CFAR algorithm when using v_{r} first in weather clutter gains detections which were not found using only Z_{v}. In clear air, the results of true detections are comparable to traditional CFAR algorithms, but the additional information from σ_{v} in the Wx-CFAR algorithm provides confidence in those detections.

Reduced False Alarm Rate

As seen in Figures 5.15(c) and 5.17(c), many of the false alarms are removed when looking at higher confidence levels. It was already shown in Table 5.2 that the false alarm rate is significantly reduced when increasing confidence. The significant reduction of false alarm rate when using a large P_{FA} is beneficial to identifying the detections gained by the P_{FA} choice.

Another way the Wx-CFAR algorithm reduces the false alarm rate is the way in which the algorithm determines a detection. By using a decision tree based on whether there is clear air or weather clutter, it can optimize the variables used for detection based on known facts about the behavior of weather clutter, clear air, and point targets in each variable. If all variables were checked and the confidence of the detection was based on the overall results, significantly more false alarms would arise. Consider the case where the weather clutter has a particularly high Z_{v}, which may also have a variation in σ_{v}. Without the presence of a point target, the v_{r} should remain similar to the surrounding storm and not provide a detection in the Wx-CFAR algorithm. If all variables were checked, however, this clutter point may appear as a target to the algorithm. The algorithm instead chooses the optimal variable in both weather clutter and clear air which has the most detections, and additional false alarms are avoided.

Variable Weights

The determined weights for the algorithm also benefit the Wx-CFAR algorithm. When determining the weights of each variable, both the number of detections and the false alarm rate were considered. For example, v_{r} has the most detections in weather clutter so it has the highest weight in that scenario, but it is not included at all for clear air. σ_{v} was able to detect in both weather clutter and clear air for the single target scenarios, and in clear air for the multiple target scenarios, but has a high false alarm rate when compared to the others, so the weight was determined to be in between that of v_{r} and Z_{v}. The weight for Z_{v} is the smallest in weather clutter because it does not detect weak targets, and only sometimes detects stronger targets. Its false alarm rate is very low, so in clear air the weight became much larger for Z_{v} while it remained the same for σ_{v}. These weights were determined using a heuristic method. These weights help reduce false alarms by putting more emphasis on the variables with fewer false alarms and more detections.

5.2.4 Limitations of the Wx-CFAR Algorithm

During the analysis of various scenarios, a few limitations of the Wx-CFAR algorithm were identified. These limitations arise when the v_{r} of the point target is similar to that of the weather clutter or when the point target is located along a clutter edge. The limitations and results for each scenario will be discussed.

Table 5.5: Results of Detection of Various Single Target Scenarios with Similar Velocity to the Weather Clutter

Velocity	P_{FA}	Z_{v}	σ_{v}	v_{r}
$\sim 0\ m\,s^{-1}$	10^{-1}	D	N	N
$\sim 0\,m\,s^{-1}$	10^{-2}	P	N	N
$\sim 23\,m\,s^{-1}$	10^{-1}	N	N	N
$\sim 23\,m\,s^{-1}$	10^{-2}	N	N	N

Similar v_{r}

The first limitation of the algorithm is found when the v_{r} of the point target is similar to that of the weather clutter. The Wx-CFAR algorithm first checks v_{r} when there is weather clutter present, which leads to missed detections that may have been found otherwise with Z_{v}. Table 5.5 shows the results of two such targets. The first has a v_{r} of about $0\ m\,s^{-1}$ with the weather clutter ranging from approximately $0\ m\,s^{-1}$ to $20\ m\,s^{-1}$. This target is detected with Z_{v}, but not v_{r} or σ_{v}. The second target has a v_{r} of around $23\ m\,s^{-1}$ with the weather clutter ranging from approximately $0\ m\,s^{-1}$ to $20\ m\,s^{-1}$. This is a simulated target with a weak signal power, and is not detected by any algorithm.

The first target identified, located at approximately $0\ m\,s^{-1}$, is also affected by the GMAP-TD filter. Table 5.5 shows the detection results when the filter is applied. If the filter is removed, the target is also detected in v_{r}, and therefore detected by the Wx-CFAR algorithm. There is an additional partial detection with σ_{v} when the filter is removed. However, removing this filter also lets in potential additional false alarms from ground clutter. The PSD of the target before and after filtering can be seen in Figures 5.18(a) and 5.18(b). In Figure 5.18(b) the target is not completely filtered out, but becomes much weaker in comparison to the weather clutter. This makes it harder to locate with the clutter present. There is an additional target at this point, moving at a v_{r} of approximately -20

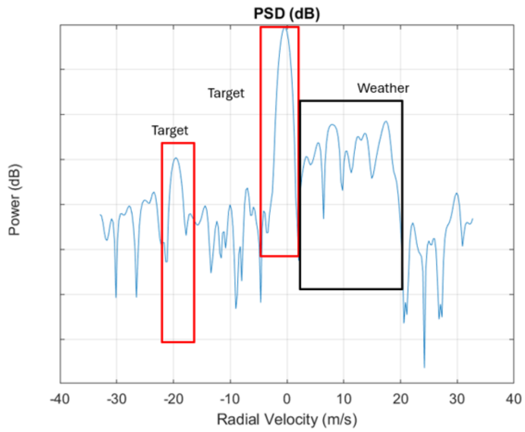

(a)

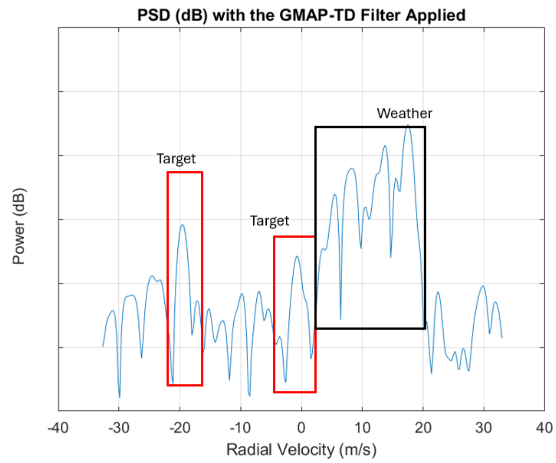

(b)

Figure 5.18: PSDs of a point target at a similar v_r to the surrounding weather clutter. Figure 5.18(a) shows the PSD without the GMAP-TD filter applied, where the target located at ~ 0 $m\,s^{-1}$ is present. Figure 5.18(b) shows the PSD with the GMAP-TD filter applied, where the target is still visible but significantly weaker due to filtering. The targets are identified in red boxes, with the weather clutter in black boxes.

$m\,s^{-1}$. This target aids in making the target more detectable in v_r when no filtering is applied. With filtering, the calculated v_r is 13.95 $m\,s^{-1}$. Without filtering, it is 1.27 $m\,s^{-1}$. This is due to the large weight around 0 $m\,s^{-1}$ from the analyzed target, but also from the additional target. The surrounding area is approximately 12.5 $m\,s^{-1}$ to 13.5 $m\,s^{-1}$ without filtering, and 13.5 $m\,s^{-1}$ to 14.5 $m\,s^{-1}$ with filtering. It is clear that when filtering is applied, this target will blend in with the surrounding weather clutter.

The second target identified, located at approximately 23 $m\,s^{-1}$, is a weak target. This target is located in weather clutter and not identified by any variable, as seen in Table 5.5. Figure 5.19 shows the PSD of the target. The target blends in with the weather clutter, being at both a similar signal strength and v_r to the weather clutter. This makes it difficult to detect with any variable.

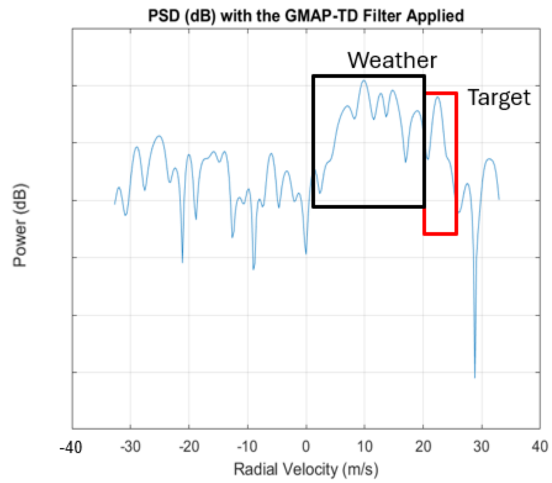

Figure 5.19: The PSD of a point target at a similar v_r to the surrounding weather clutter. The target is identified in the red box, with the weather clutter in the black box.

Table 5.6: Results of Detection of Targets Along a Clutter Edge in Clutter

-	Z_v	v_r	σ_v	Wx-CFAR
Target 1	D	D	N	2.5
Target 2	N	D	N	1.5
Target 3	N	D	N	0
Target 4	N	D	N	0

Clutter Edge

The second limitation of the Wx-CFAR algorithm is when a target is located along the clutter edge between clear air and the weather clutter. Table 5.6 shows the results of various targets located along the clutter edge which are primarily in clutter. All four targets are found using v_r, but the Wx-CFAR algorithm is not detecting two of the targets. For the cases in which the algorithm is not detecting the targets, the clutter edge is appearing as clear air to the algorithm.

Conversely, there is the case in which targets are near a clutter edge but actually located in clear air. For this instance, sixteen targets were identified with varying results. Two of these targets were not detected by any variable. Table 5.7 shows the results for the identified

Table 5.7: Results of Detection of Targets Near a Clutter Edge in Clear Air

-	Z_{v}	v_{r}	σ_{v}	Wx-CFAR
Target 1	D	N	N	0
Target 2	D	N	N	2.5
Target 3	D	N	N	2.5
Target 4	N	N	N	0
Target 5	D	N	N	0
Target 6	D	N	N	2.5
Target 7	D	N	D	3.75
Target 8	N	N	D	0
Target 9	D	N	D	3.75
Target 10	D	N	D	3.75
Target 11	D	N	D	3.75
Target 12	D	N	D	3.75
Target 13	D	N	D	3.75
Target 14	D	N	D	3.75
Target 15	D	N	D	3.75
Target 16	N	N	N	0

targets. Of these targets, eleven were detected with a confidence of at least 2.5. Two targets were detected by Z_{v} only, but the algorithm estimated that they were located in clutter rather than clear air and used the 'no detection' result from v_{r} instead. An additional target was detected in σ_{v} but not Z_{v}, resulting in a confidence of 0 regardless of if the algorithm identified clear air or weather clutter.

It is possible to increase detections by the Wx-CFAR algorithm in both scenarios by changing the requirements for clear air. To estimate if the CUT is in clear air, the algorithm checks if approximately 90% of the cells in the training band are at a power less than or equal to 1.3 times the noise power. It is possible to gain detections of the third and fourth target in Table 5.6 by being more strict with the allowed power level that is considered clear air. However, detections of targets in Table 5.7 were lost. To gain detections in this case, it was also possible to reduce the number of targets in the training band required to be considered clear air from 90%. Again, detections in the other scenario were lost when this was implemented. Therefore, the algorithm is limited in the case of a clutter edge and will lose detections in at least one of the identified cases. If it is not known whether targets will be in clear air or weather clutter when near a clutter edge, the algorithm will lose detections for one or both scenarios. If the user is expecting one scenario over another, then the algorithm can be optimized to better detect in that scenario with the understanding that more, if not all, targets in the other scenario will be lost.

5.3 Summary

Various targets in differing scenarios were identified within the data, and the ability of each individual variable and the Wx-CFAR algorithm to detect them were analyzed. The false alarm rate of the algorithms is discussed, and the improvement of the Wx-CFAR algorithm in mitigating false alarms is shown. Other benefits of the algorithm, including the confidence in detections and the ability to distinguish between weather clutter and clear air, are demonstrated. Limitations of the algorithm, including scenarios where point targets have the same or similar v_{r} to the weather clutter, and targets located near a clutter edge, are discussed with results. The next chapter will provide concluding remarks on the Wx-CFAR algorithm with an overall view of the setup and performance. Furthermore, various future work will be identified.

Chapter 6

Conclusions and Future Work

6.1 Conclusions

The MPAR project outlined specific goals for the future of phased array radar in order to combine the operational radar for various agencies into one radar. This would combine aircraft and weather radar into one, if successful. Three key capabilities for the proposed radar were defined to be ATC, weather surveillance, and non-cooperative air surveillance [8]. The Horus radar made by the ARRC is proposed as a potential solution for this project. To demonstrate the abilities of Horus, this research aims to detect point targets located in weather clutter by combining knowledge of weather variables. The key goals with this were to maintain valuable weather data while also improving point target detection techniques in a complex environment. Specifically, improving the number of detections with large amounts of clutter present and reducing false alarms were important to the detection algorithm.

Before the proposed Wx-CFAR algorithm was presented, Chapter 2 gave an overview of weather radar signals, including the overall signal flow of the radar and the derivations of the radar equation for a point target, the weather radar equation, and equations for the single polarization and dual polarization weather variables. Then, the core concepts of detection, including P_D, P_{FA}, and required SNR, were discussed in Chapter 3. CFAR algorithms for various techniques were presented, including those utilized in the Wx-CFAR algorithm, and the impact of clutter on a point target was explained.

Chapter 4 provided information on the data used and the various techniques utilized. Collected data with weather clutter and numerous targets were used to prove the effectiveness of using weather variables other than power for detection. Individual algorithms involving Z_{v}, v_{r}, and σ_{v} were created to determine the strengths and weaknesses of each variable. The Wx-CFAR algorithm was then developed to combine the weather variables to improve detection. This algorithm uses a decision tree to determine if the CUT is located in clear air or weather clutter, and then chooses the variable which is the most likely to detect it depending on the scenario. If that variable provides a detection, additional variables are used to adjust the confidence based on the results they provide.

In Chapter 5, various target scenarios were identified, including single and multiple target cases located in both clear air and weather clutter. The results showed that v_{r} worked best in weather clutter, while Z_{v} worked best in clear air. Additionally, σ_{v} was able to identify targets in both scenarios, but had a high false alarm rate, making it difficult to utilize as the primary variable. The Wx-CFAR algorithm was able to detect point targets at a better rate than just one individual variable. Furthermore, false alarms were reduced by the decision tree approach even at the lowest confidence level, and further reduced when looking only at higher confidence detections. The decision tree approach also allowed for an increase of detections in the algorithm, by utilizing the variables which detected the most targets in each scenario. The use of v_{r} in weather clutter provided additional detections for targets with a weaker signal strength than the weather clutter, which were not located with the traditional CFAR algorithm. Some limitations of the algorithm arose when the v_{r} of the point target was similar to that of the weather clutter, and additionally when the targets were located near the clutter edge. For targets near the clutter edge, two scenarios were identified: the first where the target was located inside the clutter, and the latter where the target was located in clear air. It was possible to improve the performance of the algorithm for one scenario at the cost of the performance in the other scenario.

6.2 Future Work

Although the utility of the Wx-CFAR algorithm has been proven for various limited cases, there is additional work that should be recommended. The primary desire is to collect dual-polarization data, which would allow for the algorithm to be expanded to include variables Z_{DR} and ρ_{hv}. These variables may prove particularly useful in weather clutter, as the expected value for non-meteorological echoes differs greatly from the typical meteorological values, as discussed in Chapter 2. One of the challenges with dual-polarization data will be finding threshold levels to distinguish between biological scatterers and the hard target. Additionally, further multiple-target cases where the v_{r} varies from target to target is also desired. The data used were limited in the multiple-target cases because of the similarities in σ_{v} across targets and weather clutter. Variation in target v_{r} would provide further analysis on the effectiveness of σ_{v} in the scenarios analyzed.

Apart from incorporation of dual-polarization variables, further future work for the project includes improvements to the Wx-CFAR algorithm. Artificial intelligence and machine learning may be beneficial in better determining whether the CUT is located in clear air or weather clutter in order to optimize the algorithm in the event of a clutter edge and remove this limitation. It may also be useful to change the OS-CFAR algorithm used for Z_{v} to provide more detections with this variable. With dual polarization data, incorporation of additional weather variables is possible, which could further expand the algorithm to have additional confidence levels. Additionally, the weights for each variable could potentially be improved based on results from this data.

Another future goal is to implement a tracking algorithm based on the detections from the Wx-CFAR algorithm. The first step in air surveillance is detection, followed by tracking. It has been proven that Horus is capable of both weather surveillance and point target detection, so it follows that point target tracking is the next step. With tracking implemented, the requirements of the MPAR program will be fully covered.

References

[1] M. I. Skolnik, *Introduction to Radar Systems*, 3rd ed. McGraw Hill, 2001.

[2] R. J. Doviak and D. S. Zrnic, *Doppler radar and weather observations*. Dover Pub., 2006.

[3] R. C. Whiton, P. L. Smith, S. G. Bigler, K. E. Wilk, and A. C. Harbuck, "History of operational use of weather radar by U.S. weather services. part I: The pre-NEXRAD era," *Weather and Forecasting*, vol. 13, 1998. DOI: https://doi.org/10.1175/1520-0434(1998)013⟨0219:HOOUOW⟩2.0.CO;2.

[4] A. V. Ryzhkov and D. S. Zrnic, *Radar Polarimetry for Weather Observations*. Springer, 2019.

[5] Federal Aviation Administration, *Air traffic control*, https://www.faa.gov/about/history/photo_album/air_traffic_control.

[6] Federal Aviation Administration, *A brief history of the FAA*, https://www.faa.gov/about/history/brief_history.

[7] Federal Aviation Administration, *Airport surveillance radar (ASR-11)*, https://www.faa.gov/air_traffic/technology/asr-11.

[8] O. F. C. M. Joint Action Group for Phased Array Radar Project, "Federal research and development needs and priorities for phased array radar," Jun. 2006.

[9] J. E. Stailey and K. D. Hondl, "Multifunction phased array radar for aircraft and weather surveillance," *Proceedings of the IEEE*, vol. 104, no. 3, pp. 649–659, 2016.

[10] R. D. Palmer *et al.*, "Horus— A fully digital polarimetric phased array radar for next-generation weather observations," *IEEE Transactions on Radar Systems*, vol. 1, pp. 96–117, 2023. DOI: 10.1109/TRS.2023.3280033.

[11] J. Heimmer, "Multi-mission phased array radar (MPAR) national radar R&D project," in *2008 IEEE Long Island Systems, Applications and Technology Conference*, 2008, pp. 1–2. DOI: 10.1109/LISAT.2008.4638945.

[12] C. Fulton *et al.*, "Cylindrical polarimetric phased array radar: Beamforming and calibration for weather applications," *IEEE Transactions on Geoscience and Remote Sensing*, vol. 55, no. 5, pp. 2827–2841, 2017.

[13] E. Kowalski, D. Conway, A. Morris, and C. Parry, "Multifunction Phased Array Radar Advanced Technology Demonstrator (MPAR ATD) Nearfield Testing and Fielding," in *2019 IEEE Radar Conference (RadarConf)*, ISSN: 2375-5318, Apr. 2019, pp. 1–4. DOI: 10.1109/RADAR.2019.8835837.

[14] M. Yeary, R. Palmer, C. Fulton, J. Salazar, and H. Sigmarsson, "Recent advances on an S-band all-digital mobile phased array radar," in *2019 IEEE International Symposium on Phased Array System & Technology (PAST)*, IEEE, 2019, pp. 1–5.

[15] T. D. Crum and R. L. Alberty, "The WSR-88D and the WSR-88D operational support facility," *Bulletin of the American Meteorological Society*, vol. 74, no. 9, pp. 1669–1688, 1993.

[16] NOAA, https://www.noaa.gov/jetstream/reflectivity.

[17] M. Kumjian, "Principles and applications of dual-polarization weather radar. Part I: Description of the polarimetric radar variables," *Journal of Operational Meteorology*, pp. 226–242, 2013. DOI: http://dx.doi.org/10.15191/nwajom.2013.0119.

[18] M. A. Richards, *Fundamentals of Radar Signal Processing*. McGraw Hill Education, 2022.

[19] D. A. Schnidman, "Determination of required SNR values," *IEEE Transactions on Aerospace & Electronic Systems*, vol. AES38, 2002. DOI: 10.1109/TAES.2002.1039422.

[20] F. Gini and M. Rangaswamy, *Knowledge Based Radar Detection, Tracking, and Classification*. Wiley-Interscience, 2008.

[21] H. Rohling, "Ordered statistic CFAR technique - an overview," in *2011 12th International Radar Symposium (IRS)*, ISSN: 2155-5753, Sep. 2011.

[22] V. V. Tien, T. V. Hop, L. H. Nam, N. V. Loi, and T. T. Thanh, "An adaptive 2D-OS-CFAR thresholding in clutter environments: Test with real data," in *2018 5th International Conference on Signal Processing and Integrated Networks*, 2018. DOI: https://doi.org/10.1109/SPIN.2018.8474143.

[23] H. Madjidi, T. Laroussi, and N. Detouche, "Two-sided automatic censoring CFAR detector based on the interquartile range in a heterogeneous Weibull clutter," *Physical Communication*, vol. 65, 2024. DOI: https://doi.org/10.1016/j.phycom.2024.102396.

[24] P. Stoica and R. Moses, *Spectral Analysis of Signals*. Prentice Hall, 2005.

[25] F. Robey, *DARPA BLiP program*, https://www.darpa.mil/research/programs/beyond-linear-processing.

[26] M. Yeary, D. Schvartzman, M. Herndon, R. D. Palmer, B. Epstein, and F. Robey, "Fully digital horus radar experiments in support of DARPA's beyond linear processing program," in *2024 IEEE International Symposium on Phased Array Systems and Technology (ARRAY)*, 2024. DOI: https://doi.org/10.1109/ARRAY58370.2024.10880425.

[27] J. V. DiFranco and W. L. Rubin, *Radar Detection*. SciTech Publishing, Inc., 2004.

[28] C. M. Nguyen and V. Chandrasekar, "Gaussian model adaptive processing in time domain (GMAP-TD) for weather radars," *Journal of Atmospheric and Oceanic Technology*, 2013. DOI: https://doi.org/10.1175/JTECH-D-12-00215.1.

[29] W. Li, J. Zhang, L. Liu, J. Zhou, Q. Sui, and H. Li, "CFAR algorithm based on different probability models for ocean target detection," *IEEE Access*, vol. 9, 2021. DOI: 10.1109/ACCESS.2021.3126003.

[30] Z. Yang, Y. Lai, H. Zhou, Y. Tian, Y. Qin, and Z. Lv, "Improving ship detection based on decision tree classification for high frequency surface wave radar," *Journal*

of Marine Science and Engineering, vol. 11, 2023. DOI: https://doi.org/10.3390/jmse11030493.

Appendix A

Acronyms

ACF Autocorrelation Function

ARRC Advanced Radar Research Center

ARTS Automated Radar Traffic Control System

ASR-1 Airport Surveillance Radar-1

ASR-11 Airport Surveillance Radar-11

ATC Air Traffic Control

ATD Advanced Technology Demonstrator

BLiP Beyond Linear Processing

CA-CFAR Cell-Averaging Constant False Alarm Rate

CFAR Constant False Alarm Rate

CPI Coherent Processing Interval

CPPAR Cylindrical Polarimetric Phased Array Radar

CUT Cell Under Test

DARPA Defense Advanced Research Projects Agency

DFT Discrete Fourier Transform

FAA Federal Aviation Administration

GMAP-TD Gaussian Model Adaptive Processing in Time Domain

H Horizontal Polarization

IQ In-Phase and Quadrature

IQR Interquartile Range

IQR-CFAR Interquartile Range Constant False Alarm Rate

LFM Linear Frequency Modulated

LRT Likelihood Ratio Test

MPAR Multifunction Phased Array Radar

MSL Mean Sea Level

NOAA National Oceanic and Atmospheric Administration

OS-CFAR Ordered Statistics Constant False Alarm Rate

PDF Probability Density Function

PPI Plan Position Indicator

PRT Pulse Repetition Time

PSD Power Spectral Density

RCS Radar Cross Section

ROC Radar Operating Characteristics

STALO Stable Local Oscillator

SNR Signal-to-Noise Ratio

USAF United States Air Force

V Vertical Polarization

WSR-88D Weather Surveillance Radar-1988 Doppler

Wx-CFAR Weather-Aware Constant False Alarm Rate